



## Available online at www.sciencedirect.com

## **ScienceDirect**

Comput. Methods Appl. Mech. Engrg. 318 (2017) 667–700

Computer methods in applied mechanics and engineering

www.elsevier.com/locate/cma

# Computational thermo-hydro-mechanics for multiphase freezing and thawing porous media in the finite deformation range

SeonHong Na, WaiChing Sun\*

Department of Civil Engineering and Engineering Mechanics, Fu Foundation School of Engineering and Applied Science Columbia University in the City of New York, 614 SW Mudd, Mail Code: 4709, New York, NY 10027, United States

Received 13 September 2016; received in revised form 28 December 2016; accepted 24 January 2017 Available online 7 February 2017

#### **Highlights**

- A finite strain formulation for frozen porous media based on multiplicative kinematics is presented.
- The stabilization procedure and pre-conditioner for the three-phase frozen soil are adopted.
- Nonlocal diffusion-deformation coupling effects during freezing and thawing are analyzed.

## **Abstract**

A stabilized thermo-hydro-mechanical (THM) finite element model is introduced to investigate the freeze-thaw action of frozen porous media in the finite deformation range. By applying the mixture theory, frozen soil is idealized as a composite consisting of three phases, i.e., solid grain, unfrozen water and ice crystal. A generalized hardening rule at finite strain is adopted to replicate how the elasto-plastic responses and critical state evolve under the influence of phase transitions and heat transfer. The enhanced particle interlocking and ice strengthening during the freezing processes and the thawing-induced consolidation at the geometrical nonlinear regimes are both replicated in numerical examples. The numerical issues due to lack of two-fold inf–sup condition and ill-conditioning of the system of equations are addressed. Numerical examples for engineering applications at cold region are analyzed via the proposed model to predict the impacts of changing climate on infrastructure at cold regions.

© 2017 Elsevier B.V. All rights reserved.

Keywords: Finite strain thermo-hydro-mechanics; Poromechanics; Generalized hardening rule; Critical state; Stabilization procedure

#### 1. Introduction

In permafrost regions, soil underneath pavement and concrete structures may experience freeze—thaw action. During the freezing phase, the crystallization of ice leads to the expanding of voids and micro-cracks in the porous media. When temperature arises, ices near the heat source may thaw out and turn into meltwater, but this water may be

<sup>\*</sup> Corresponding author. Fax: +1 212 854 6267. E-mail address: wsun@columbia.edu (W. Sun).

trapped by the frozen region that remains nearly impermeable. This results in a thaw-weaken soil that is wet, loose and highly deformable [1–4]. The freeze–thaw action may repeat itself everyday due to the temperature difference between day and night near surface, and, in the larger spatial and time scales, between winter and spring. The accumulated damage and deterioration of roads, airfields and infrastructure due to freeze–thaw action are of ultimate importance for vehicle mobility and structural integrity of infrastructure in cold region. This demand of understanding the freeze–thaw action of porous media undergoing large deformation is further intensified by the climate changes that bring in more extreme weather and heavier rains which are expected to accelerate the damages of infrastructure in alerting speed in the coming decades. For instance, the frost-free season in Fairbanks, Alaska has been lasted 50% longer between 1904 and 2008. The increase of permafrost temperature, which occurs throughout Alaska since the late 1970s, has caused land subsidence and put public infrastructure, such as roads, runways and sewer system, at risk [4,5].

In this paper we present for the first time a finite strain poromechanics theory that fully considers the thermohydro-mechanical coupling effect of the mass-exchanging, phase-transiting porous media. Previously, significant contributions have been made to derive thermal-sensitive or degree-of-saturation-sensitive constitutive laws for the frozen soil [6]. These constitutive laws are often incorporated in thermo-mechanical simulations in which the presence of unfrozen water is neglected. A notable exception is the work presented in [7] where the infinitesimal strain thermo-hydro-mechanical model is coupled with a modified Cam-clay model with generalized hardening rules. Unlike the previous modeling efforts in which the flow of unfrozen water, energy dissipation due to phase transition and geometrical nonlinearity are neglected (cf. [6,8,9]), we introduce a new comprehensive theory that incorporates all of these important thermo-hydro-mechanical mechanisms into the balance principles (linear momentum, mass, energy) in the finite deformation range. An implicit total Lagrangian finite element framework is formulated, while thermal and cryo-suction effects are explicitly captured by a generalized hardening rules that allow the yield surface to evolve based on the volume fraction of ices in the pore space and the temperature. In addition, we also highlight a number of numerical issues that are crucial for developing a practical and robust numerical implementation. Numerical examples are provided for elucidating the mechanical behavior of frozen soil under thawing and freezing conditions. The results indicate that a comprehensive model that explicitly captures the multiple thermo-hydro-mechanical coupling mechanisms of frozen porous media (instead of lumping them together through phenomenological laws) may yield far more accurate and reliable results. This elegant approach also eliminates the needs to introducing excessive amount of ad hoc parameters solely for curve-fitting, and is therefore easier to calibrate and more practical.

The organization of the paper is as follows. We first provide the derivation of the balance principle for frozen soil in the geometrically nonlinear regime (Section 2). Then, the finite strain elasto-plasticity model with the non-mechanical hardening rule and the finite strain suction-permeability theory is presented (Section 3). Following this is the total Lagrangian finite element formulation of the thermo-hydro-mechanical model (Section 4). The numerical stability, in particular, the two-fold inf–sup condition and the corresponding two-fold inf–sup test are outlined in Section 5. Numerical examples are then provided (Section 6), followed by a conclusion.

As for notations and symbols, bold-faced letters denote tensors; the symbol '·' denotes a single contraction of adjacent indices of two tensors (e.g.,  $\mathbf{a} \cdot \mathbf{b} = a_i b_i$  or  $\mathbf{c} \cdot \mathbf{d} = c_{ij} d_{jk}$ ); the symbol ':' denotes a double contraction of adjacent indices of tensor of rank two or higher (e.g.,  $\mathbf{C} : \mathbf{\epsilon}^e = C_{ijkl} \mathbf{\epsilon}^e_{kl}$ ); the symbol '⊗' denotes a juxtaposition of two vectors (e.g.,  $\mathbf{a} \otimes \mathbf{b} = a_i b_j$ ) or two symmetric second order tensors (e.g.,  $(\mathbf{a} \otimes \mathbf{\beta}) = \alpha_{ij} \beta_{kl}$ ). As for sign conventions, unless specify otherwise, we consider the direction of the tensile stress and dilative pressure as positive.

#### 2. Conservation laws

In this section, we present the balance principle (i.e., balance of linear momentum, mass and energy) for frozen soil undergoing finite deformation. The soil is idealized as a continuum mixture that consists of three constituents, the liquid water and crystal ice, which occupy the pores inside the solid skeleton, and the solid constituent that forms the solid skeleton. Based on the classical thermo-hydro-mechanics theory as reported in the previous studies (e.g., [2,10–15]), we present a new derivation that takes account of the heat generated from plastic dissipation and the thermal-convection to replicate the path-dependent thermo-hydro-mechanical effect of frozen porous media with infiltrating unfrozen water in the finite deformation range. The incorporation of geometrical nonlinearity effect is critical for modeling thawing materials in which the cryo-suction effect often leads to soft soil that develops large strain. The energy required for the phase transition between ice and water is incorporated into the balance of energy. Meanwhile we adopt the Taylor–Quinney coefficient to control the amount of mechanical dissipation converted into heat. We extend both the net stress theory in [16] and the effective stress theory in [12] for the finite strain problems.

Consequently, the energy dissipation due to fluid diffusion, thermal convection, phase transition and outward heat flux are all formulated in the total Lagrangian framework. The implications of these modifications will be examined via numerical examples.

## 2.1. Kinematics of three-phase frozen porous media

We consider an idealized kinematics based on the theory of pre-melting dynamics which elucidates the mechanism of existence of unfrozen water at temperatures below the bulk freezing point (e.g., [3,17]). In addition, the behavior of crystal ice is captured through crystal ice pressure obtained by the Clausius–Clapeyron equation (29). This relation is based on thermodynamic requirements for equilibrium that needs to be satisfied by crystal ice pressure, liquid water pressure and temperature in non-isothermal condition [7,18]. Within this framework, we adopt the passive air phase assumption. Hence, we neglect the existence of air in the pore space and consider a three-phase porous medium composed of solid skeleton, liquid water, and crystal ice [19,20]. Based on the mixture theory, if the representative elementary volume exists, then the three-phase material can be idealized as a mixture continuum where each constituent occupies a fraction of volume at the same macroscopic material point (e.g., [21–25]). Unlike solid composite in which one may assume that all constituents at a material point share the same trajectories until delamination or other forms of failure, the solid and pore-fluid constituents do not necessarily follow the same trajectory unless the porous medium is locally undrained. Therefore, the mappings for materials at a point x of the current configuration can be represented from the configuration of solid skeleton (X), liquid water (X) and crystal ice (X) counterparts:

$$\mathbf{x} = \varphi^{\alpha} \left( \mathbf{X}^{\alpha}, t \right), \quad \alpha = \mathbf{S}, \, \mathbf{L}, \, \mathbf{C}.$$
 (1)

Because the path-dependent constitutive laws and the internal variables that represent the loading history of the solid skeleton are corresponding to the solid skeleton trajectory, our formulation will be derived in accordance with the motion of the solid skeleton ( $\varphi^S$ ). As a result, the motion of liquid water and crystal ice in THM model at finite-strain is captured by their relative motion with respect to the solid skeleton. The frozen soil with three constituents (solid skeleton (S), liquid water (L) and crystal ice (C)) is homogenized as a continuum. Therefore, the current density field of a porous medium can be written as,

$$\rho = \rho^{S} + \rho^{L} + \rho^{C} = \phi^{S} \rho_{S} + \phi^{L} \rho_{L} + \phi^{C} \rho_{C}, \tag{2}$$

where  $\rho^{\alpha}$  ( $\alpha=S,L,C$ ) is the partial mass density of constituent  $\alpha$  given by  $\rho^{\alpha}=\phi^{\phi}\rho_{\alpha}$ ;  $\phi^{\alpha}$  is the volume fraction of each constituent in the current configuration;  $\rho_{\alpha}$  is the intrinsic mass density of each constituent  $\alpha$ . By assuming that the pores inside the solid skeleton are fully saturated with either liquid water or crystal ice, the density of frozen soil mixture can be obtained by taking the freezing characteristic function. The freezing characteristic function ( $S_L$ ) indicates the ratio between the volume of liquid water in the void to the total volume of the void, while the ratio of crystal ice in the total void space is  $S_C=1-S_L$ . The concept of freezing characteristic function is analogous to the water retention curve of unsaturated porous materials (in Section 3.2). Therefore, the total current density of Eq. (2) can be also rewritten as.

$$\rho = \phi^{S} \rho_{S} + \phi^{L} S_{I} \rho_{I} + \phi^{L} S_{C} \rho_{C} = (1 - \phi^{L}) \rho_{S} + \phi^{L} [S_{I} \rho_{I} + (1 - S_{I}) \rho_{C}]. \tag{3}$$

Note that this becomes the total current density of a fully saturated porous medium under unfrozen state when  $S_L$  becomes a unity (the pores are fully saturated only with liquid water).

## 2.2. Balance of linear momentum

To capture the stress status during thawing and freezing, we adopt the Bishop's effective stress theory for the frozen soil idealized as a three-phase continuum [26]. In other words, we assume that the total stress can be partitioned into the effective stress  $\sigma'$  which evolves due to the deformation and loading history of the solid skeleton, and a net pore pressure  $\bar{p}$  build up in the void space due to the motion and interaction of the water and ice crystal, that is,

$$\sigma = \sigma' - \bar{p}I$$
, with  $\bar{p} = \chi p_{L} + (1 - \chi)p_{C}$ , (4)

where the parameter  $\chi$  is commonly assumed to be equal to the degree of liquid saturation ( $\chi = S_L$ ) (e.g., [27–29]) where  $p_L$  and  $p_C$  indicate the liquid water and crystal ice pressures, respectively. This treatment is a simplification of the actual retention behavior in which the history or path dependence of the effective stress coefficient  $\chi$  is neglected. In this formulation, the interaction of the ice crystal and unfrozen water is characterized by a freezing retention curve in an analogy of the characterization of the water-air interaction via the water retention curve (cf. [30,31]). As such, the pore space is assumed to be always saturated by a combination of two constituents, the ice crystal and unfrozen water. Furthermore, we follow the treatment in [7] and [32] where the Bishop's effective stress principle originally proposed for unsaturated porous media is applied to capture the interaction among the solid skeleton, ice crystal and unfrozen water. It should be noted that while the usage of freezing retention curve and Bishop's effective stress theory does imply that the water-ice-skeleton and water-air-skeleton interactions share similarities, in particular, both of them are determined by pore size distribution and the water-solid interface tensional force [2,7,16,27], the ice crystal is not considered as a fluid, and the influence of the presence of ice on the shear strength must be taken account properly. In this work, this influence is captured via a phenomenological approach in the framework of finite strain critical state theory. More consistent approach may require more explicit modeling of the crystallization of ice phase at the pore scales and treating the ice and solid skeleton as a composite or effective medium composed of two solid phases [32]. These improvements are out of the scope of this study but will be considered in future extensions. In this work, we adopt the total Lagrangian formulation and hence the model is formulated with respect to the reference configuration of the solid skeleton. Note that the total Lagrangian formulation is not the only feasible choice. For instance, Sanavia et al. [33] have successfully formulated the poromechanics problem in a spatial setting which results in an updated Lagrangian formulation. Due to the usage of total Lagrangian formulation in our current work, the balance of linear momentum is written in terms of the total Piola-Kirchhoff stress tensor, which is related to the first effective Piola-Kirchhoff stress tensor and the pull back of the contribution from the water and ice crystal constituents, i.e.,

$$P = \tau \cdot F^{-T} = \tau' \cdot F^{-T} - J \bar{p} F^{-T}, \tag{5}$$

where  $\tau = J\sigma$  is the symmetric total Kirchhoff stress tensor,  $\tau' = J\sigma'$  is the effective Kirchhoff stress tensor (e.g., [34–38]). Therefore, by ignoring the inertia forces, the balance of linear momentum in Lagrangian form takes the following relation in the reference configuration:

$$\nabla^X \cdot \mathbf{P} + \rho_0 \mathbf{G} = 0, \tag{6}$$

where  $\rho_0 = J\rho$  is the pullback of the total mass density which can be determined via Eq. (3).

#### 2.3. Balance of mass

We assume that the porous medium is fully saturated with three constituents, solid (S), liquid water (L) and crystal ice (C). The possibility of phase transition between liquid water and crystal ice is considered. The following derivation is formulated with our choice of primary variables (solid displacement, liquid phase pressure, and temperature) in mind. Since the frozen porous media we considered consist of three constituents, one may also introduce additional primary variables, such as the degree of saturation or ice phase pressure. However, as we will discuss in Section 3, one may also exploit arguments from the Clausius-Clapeyron equation to eliminate the ice phase pressure from the prime variables by expressing it as a function of the liquid phase pressure and temperature. This approach allows us to derive a simplified system of equations with just three prime variables. The balance of mass for a three-phase solid-water-ice mixture, therefore, can be written as,

$$\frac{D\rho^{S}}{Dt} + \rho^{S} \nabla^{x} \cdot \mathbf{v} = 0, \tag{7}$$

$$\frac{D\rho^{L}}{Dt} + \rho^{L}\nabla^{x} \cdot \mathbf{v} + \nabla^{x} \cdot \left(\rho^{L}\mathbf{v}_{LS}\right) = -\mathring{m}_{L\to C},$$

$$\frac{D\rho^{C}}{Dt} + \rho^{C}\nabla^{x} \cdot \mathbf{v} + \nabla^{x} \cdot \left(\rho^{C}\mathbf{v}_{CS}\right) = \mathring{m}_{L\to C}.$$
(8)

$$\frac{D\rho^{C}}{Dt} + \rho^{C}\nabla^{x} \cdot v + \nabla^{x} \cdot (\rho^{C}v_{CS}) = \stackrel{\circ}{m}_{L \to C}.$$

$$\tag{9}$$

Here  $m_{L\to C}$  is the rate of liquid water mass crystallizing into ice crystal. In general, the Eulerian relative flow vector of ice with respect to soil skeleton ( $v_{CS}$ ) is much slower than that of the liquid ice. Therefore, we assume that  $v_{CS} \approx 0$ .

Combining Eqs. (8) and (9) leads to the following equation,

$$\frac{D\rho^{L}}{Dt} + \frac{D\rho^{C}}{Dt} + (\rho^{L} + \rho^{C})\nabla^{x} \cdot \mathbf{v} + \nabla^{x} \cdot (\rho^{L}\mathbf{v}_{LS}) = 0.$$

$$(10)$$

We can consider an equation of state for density/pressure relation through a barotropic flow assumption (e.g., [14,37,38]). Introducing a bulk modulus for each phase (solid, liquid water, and crystal ice), we expand the total time derivative of the partial density  $\rho^{\pi}$  as,

$$\frac{D\rho^{L}}{Dt} = \frac{D(\phi^{L}\rho_{L})}{Dt} = \rho_{L}\frac{D\phi^{L}}{Dt} + \phi^{L}\frac{D\rho_{L}}{Dt} = \rho_{L}\left(\frac{D\phi^{L}}{Dt} + \frac{\phi^{L}}{K_{L}}\frac{Dp_{L}}{Dt}\right),\tag{11}$$

likewise, 
$$\frac{D\rho^{C}}{Dt} = \rho_{C} \left( \frac{D\phi^{C}}{Dt} + \frac{\phi^{C}}{K_{C}} \frac{Dp_{C}}{Dt} \right).$$
 (12)

Inserting these relationships into Eqs. (7) and (10) gives,

$$\frac{D\phi^{S}}{Dt} + \frac{\phi^{S}}{K_{S}} \frac{Dp_{S}}{Dt} + \phi^{S} \nabla^{x} \cdot \mathbf{v} = 0, \tag{13}$$

$$\rho_{L}\left(\frac{D\phi^{L}}{Dt} + \frac{\phi^{L}}{K_{L}}\frac{Dp_{L}}{Dt}\right) + \rho_{C}\left(\frac{D\phi^{C}}{Dt} + \frac{\phi^{C}}{K_{C}}\frac{Dp_{C}}{Dt}\right) + (\rho^{L} + \rho^{C})\nabla^{x} \cdot \mathbf{v} + \nabla^{x} \cdot (\rho^{L}\mathbf{v}_{LS}) = 0.$$

$$(14)$$

Taking into account the saturation of liquid water and crystal ice, we use the following identity:

$$\frac{D\phi^{\pi}}{Dt} = \frac{D}{Dt} \left[ S_{\pi} (1 - \phi^{S}) \right]$$

$$= (1 - \phi^{S}) \frac{DS^{\pi}}{Dt} - S_{\pi} \frac{D\phi^{S}}{Dt}, \qquad \pi = L, C, \tag{15}$$

in which,  $S_L$  is the saturation of liquid water and  $S_C$  (=1 –  $S_L$ ) is the saturation of crystal ice. Combining the equations of (13), (14), and (15) leads to an expression for the mass balance equation of three-phase porous medium. Note the notation that  $(\dot{\cdot}) = D(\cdot)/Dt$  is used.

$$\rho_{L} \left[ (1 - \phi^{S}) \dot{S}_{L} + \frac{\phi^{L}}{K_{L}} \dot{p}_{L} + \frac{S_{L} \phi^{S}}{K_{S}} \dot{p}_{S} + S_{L} \nabla^{x} \cdot \boldsymbol{\nu} \right]$$

$$+ \rho_{C} \left[ (1 - \phi^{S}) \dot{S}_{C} + \frac{\phi^{C}}{K_{C}} \dot{p}_{C} + \frac{S_{C} \phi^{S}}{K_{S}} \dot{p}_{S} + S_{C} \nabla^{x} \cdot \boldsymbol{\nu} \right] + \nabla^{x} \cdot \boldsymbol{w} = 0,$$

$$(16)$$

where  $\mathbf{w} = \phi^{\mathrm{L}} \rho_{\mathrm{L}} \mathbf{v}_{\mathrm{LS}}$ . The Piola transform of  $\mathbf{w}$  is

$$W = JF^{-1} \cdot w, \tag{17}$$

where W and w are the Lagrangian and Eulerian relative mass flow vectors with the following Piola identity (e.g., [34–38]),

$$\nabla^X \cdot W = J \nabla^x \cdot w. \tag{18}$$

Furthermore, we note that (cf. [38]),

$$J\dot{p}_{\pi} = \overline{(Jp_{\pi})} - p_{\pi}\dot{J}, \quad \pi = S, L, C.$$
 (19)

Substituting Eqs. (17)–(19) into Eq. (16) gives the mass balance equation in the reference configuration as,

$$\rho_{L} \left[ (1 - \phi^{S}) \dot{S}_{L} J + \frac{\phi^{L}}{K_{L}} \frac{\dot{\rho}_{L} J}{p_{L} J} + \frac{S_{L} \phi^{S}}{K_{S}} \frac{\dot{\rho}_{S} J}{p_{S} J} + \left( S_{L} - \frac{\phi^{L}}{K_{L}} p_{L} - \frac{S_{L} \phi^{S}}{K_{S}} p_{S} \right) \dot{J} \right]$$

$$+ \rho_{C} \left[ (1 - \phi^{S}) \dot{S}_{C} J + \frac{\phi^{C}}{K_{C}} \frac{\dot{\rho}_{C} J}{p_{C} J} + \frac{S_{C} \phi^{S}}{K_{S}} \frac{\dot{\rho}_{S} J}{p_{S} J} + \left( S_{C} - \frac{\phi^{C}}{K_{C}} p_{C} - \frac{S_{C} \phi^{S}}{K_{S}} p_{S} \right) \dot{J} \right]$$

$$+ \nabla^{X} \cdot \mathbf{W} = 0.$$

$$(20)$$

Assuming that the change of unfrozen fluid content due to the expansion and contraction of the constituents of porous medium is negligible compared to that due to changes of porosity and degree of saturation, mass conservation equation

is simplified as,

$$(1 - \phi^{S})(\rho_{L} - \rho_{C})\dot{S}_{L}J + [\rho_{L}S_{L} + \rho_{C}(1 - S_{L})]\dot{J} + \nabla^{X} \cdot W = 0.$$
(21)

Here the Lagrangian liquid water mass flux after a pull-back operation reads (cf. [14,39]),

$$\mathbf{W} = \rho_{\mathbf{L}} \mathbf{K}_{\mathbf{L}} \cdot (-\nabla^{\mathbf{X}} p_{\mathbf{L}} + \rho_{\mathbf{L}} \mathbf{F}^{\mathbf{T}} \cdot \mathbf{G}), \quad \text{where,} \quad \mathbf{K}_{\mathbf{L}} = J \mathbf{F}^{-1} \cdot \mathbf{k} \cdot \mathbf{F}^{-\mathbf{T}}. \tag{22}$$

The pull-back permeability tensor ( $K_L$ ) is obtained by pulling-back the Eulerian effective permeability tensor to the reference configuration [37]. The constitutive law for the Eulerian effective permeability tensor (k) in Eq. (38), which depends on the degree of saturation of the ice crystal, porosity and temperature will be described in Section 3.2.

## 2.4. Balance of energy

For the sake of simplification, the previous efforts on frozen soil modeling often adopt a balance of energy equation that neglects the contribution of mechanical dissipation, heat convection, structural heating and the geometrical nonlinearity (cf. [6,7,32,40]). This treatment is often a trade-off between convenience and rigorousness. A well-justified simplification may allow one to derive analytical solution or at the very least shorten the implementation time. Nevertheless, the additional assumptions also limit the application of the simplified thermo-hydro-mechanics theory to more general situations. For instead, dissipation due to frictional shear of frozen soil may generate heat that melts the portion of ice crystal in the pore space. Flow of unfrozen water that is significantly hotter or colder than the frozen soil may cause significant change in temperature of the frozen soil, and the thawing process may weaken the soil and cause the thaw-soil highly deformable. These mechanisms are important for modeling frozen soil that exhibits path dependent behaviors, especially when the hardening/softening mechanism of the frozen soil is sensitive to the temperature [7]. These reasons above motivate us to derive a version of the balance of energy that incorporates all the aforementioned mechanisms.

Our starting point is the balance of energy for three-phase frozen soil at finite strains expressed in the current configuration which reads (cf. [14,41]):

$$Jc_{F}\dot{T} = \left[ -J\nabla^{x} \cdot \boldsymbol{q} + \frac{\phi^{L}S_{L}c_{FL}}{\rho_{L}}J\boldsymbol{w} \cdot \nabla^{x}T \right] + [D_{\text{mech}} + R_{T}]. \tag{23}$$

Here we adopt an apparent heat capacity  $c_F$ , which incorporates both the heat capacity of frozen soil and latent heat [9,42,43], that is,

$$c_{F} = c_{FS}\phi^{S} + c_{FL}(1 - \phi^{S})S_{L} + c_{FC}(1 - \phi^{S})S_{C} + \rho_{C}(1 - \phi^{S})l\frac{\partial S_{L}}{\partial T}$$

$$= \rho_{S}c_{S}\phi^{S} + \rho_{L}c_{L}(1 - \phi^{S})S_{L} + \rho_{C}c_{C}(1 - \phi^{S})S_{C} - \rho_{C}(1 - \phi^{S})l\frac{\partial S_{C}}{\partial T},$$
(24)

where  $c_{\rm S}$ ,  $c_{\rm L}$  and  $c_{\rm C}$  are the specific heats of each constituent, and l is the latent heat of fusion (liquid water and crystal ice). In Eq. (23),  $D_{\rm mech}$  denotes the contribution to the dissipation due to pure mechanical load and  $R_T$  is the heat source term. Assuming that all constituents of frozen soil follow Fourier's law, the Cauchy heat flux may be expressed as the dot product of the gradient of temperature and the effective thermal conductivity of the multi-phase porous media ( $\kappa$ ). In this work, we estimate the effective thermal conductivity as the geometric mean [44], i.e.,

$$q = -\kappa \nabla^{\mathbf{x}} T, \quad \kappa = \kappa_{\mathbf{S}}^{1-\phi^{\mathbf{S}}} \kappa_{\mathbf{L}}^{S_{\mathbf{L}}\phi^{\mathbf{S}}} \kappa_{\mathbf{C}}^{S_{\mathbf{C}}\phi^{\mathbf{S}}}, \tag{25}$$

where  $\kappa_S$ ,  $\kappa_L$  and  $\kappa_C$  indicate the isotropic thermal conductivities of solid, liquid water and crystal ice, respectively. It should be noted that the geometric mean is only one of the many possible ways to homogenize the thermal conductivity. Another valid choice can be, for instance, the estimate based on Eshelby equivalent inclusion method (cf. [14]). Applying the Piola–Kirchhoff heat flux Q corresponding Eq. (25) reads,

$$\mathbf{Q} = -\mathbf{K}_T \cdot \nabla^X T, \tag{26}$$

where  $K_T$  is the pull-back thermal conductivity tensor, that is,

$$\mathbf{K}_T = J\mathbf{F}^{-1} \cdot \boldsymbol{\kappa} \cdot \mathbf{F}^{-T}, \quad \boldsymbol{\kappa} = \kappa \mathbf{I}. \tag{27}$$

Eq. (23) can be recapitulated in the reference configuration as follows:

$$Jc_{\mathbf{F}}\dot{T} = \left[ -\nabla^{\mathbf{X}} \cdot \mathbf{Q} + \frac{\phi^{\mathbf{L}} S_{\mathbf{L}} c_{\mathbf{F}\mathbf{L}}}{\rho_{\mathbf{L}}} \mathbf{W} \cdot \mathbf{F}^{-T} \cdot \nabla^{\mathbf{X}} T \right] + [D_{\text{mech}} + R_T]$$
(28)

where  $D_{\text{mech}} = \beta S : D^P$  and  $\beta$  is the Taylor–Quinney coefficient (cf. [45–47]). Here we assume that the mechanical dissipation of the solid skeleton is primary driven by plastic work. A more comprehensive study would require the consideration of other dissipative mechanisms, such as creeping and fracture. Furthermore, it is also possible that the Taylor–Quinney coefficient of frozen soil can be temperature and strain-rate dependent. Nevertheless, the identification of the relation among the Taylor–Quinney coefficient and the temperature and strain-rate requires suitable design of experiments to generate sufficient experimental data. These generalizations of the proposed model will be considered in the future studies.

## 3. Constitutive model

The balance principle presented in Section 2 provides a general description for the three-phase frozen porous media undergoing large deformation. In this section, we introduce specific constitutive models to replicate the thermohydro-mechanical responses of a soil undergoing deformation in geometrical nonlinear regime. In particular, we assume that the soil in the unfrozen and isothermal states may exhibit constitutive responses adequately described by a finite strain Cam-Clay model with an associative hardening rule (e.g., [48,49]). We then introduce an additional hardening/softening mechanism which allows the yield surface changes according to the degree of saturation of ice crystal to mimic the tensile and enhanced shear strength due to the presence of ice crystal in the void space. This solid constitutive law is coupled with the freezing retention model, which relates the degree of saturation of ice crystal with temperature and the difference between the ice and pore water pressure.

#### 3.1. Constitutive law for skeleton with ice crystals

The finite strain solid constitutive law is derived based on the infinitesimal-strain generalized hardening model first introduced in [7] and further explained in [16]. This constitutive law has ties to the basic Barcelona model [50] and the generalized hardening rule [51,52] in the sense that yield function is expressed not only as a function of the effective stress invariants and preconsolidation pressure, but also depends on suction (and indirectly the degree of saturation). As a result, the hardening/softening of the material can be triggered by a change of the (mechanical) effective stress state as well as a change on the (non-mechanical) material state (e.g., frozen/unfrozen, chemical weathering). Here our goal is to extend this model to the finite deformation range, within the framework of multiplicative plasticity.

As explained in [53], one of the key difficulties in introducing constitutive law in the finite deformation range is the cumbersome derivation and implementation requiring proper linearization of the multiplicative kinematics. One attractive way to overcome this obstacle is to establish a formal connection between the infinitesimal-strain constitutive law and the finite-strain counterpart. This idea is not new. For instance, Simo [35] has shown that in the case of isotropic plasticity, infinitesimal constitutive law can be extended to a finite strain counterpart by adopting suitable energy conjugated measure. Borja and Tamagnini [48] introduce an algorithmic design that employs exponential/logarithmic mapping and spectral decomposition to derive the analytical consistent tangent for the Cam-Clay model. Meanwhile, Cuitino and Ortiz [53] introduce a general algorithmic design where one may create a finite-strain version of any constitutive law by embedding an infinitesimal-strain constitutive law within a three-step framework [48,53,54].

This simple and yet efficient approach is used in this study. In the implementation process, we first implement an infinitesimal-strain constitutive law with a generalized hardening rule that depends on the degree of saturation of ice crystal. Following this step, we introduce additional pre and post-processing steps. In particular, the preprocessing step allows one to employ logarithmic mapping to project finite strain measures to the infinitesimal strain counterparts such that infinitesimal-strain constitutive law is used to generate an incremental stress update. Following this step, the first effective Piola–Kirchhoff stress tensor can be obtained via the Piola transformation (cf. [53,54]). For completeness, this procedure is outlined below.

(i) *Pre-processing*. Given incremental displacement  $\Delta u$ , update the deformation gradient and compute elastic trial state as.

$$\begin{split} \boldsymbol{F}_{\Delta} &:= \boldsymbol{I} + \nabla^{\boldsymbol{X}}(\Delta \boldsymbol{u}), \quad \boldsymbol{F}_{n+1} := \boldsymbol{F}_{\Delta} \cdot \boldsymbol{F}_{n}, \quad \boldsymbol{B}_{b}^{e} := \exp\left[2\boldsymbol{\varepsilon}_{n}^{e}\right] \\ \boldsymbol{B}_{n+1}^{e \, \text{trial}} &:= \boldsymbol{F}_{\Delta} \cdot \boldsymbol{B}_{n}^{e} \cdot (\boldsymbol{F}_{\Delta})^{\text{T}}, \quad \boldsymbol{\varepsilon}_{n+1}^{e \, \text{trial}} := \frac{1}{2} \ln\left[\boldsymbol{B}_{n+1}^{e \, \text{trial}}\right]. \end{split}$$

- (ii) Infinitesimal-strain update. The general elastic predictor/return mapping algorithm using the relationship between  $\tau'$  and  $\varepsilon$ .
- (iii) Post-processing. Update the first effective Piola–Kirchhoff stress tensor (P'),

$$\boldsymbol{P}_{n+1}' = \boldsymbol{\tau}_{n+1}' \cdot \boldsymbol{F}_{n+1}^{-\mathrm{T}}.$$

Note that the relationship between  $\tau'$  and  $\varepsilon$  requires the exact calculation of derivative of logarithmic tensor or consideration of higher order terms in Taylor expansion while deriving the consistent tangent stiffness matrix (in Section 4.2).

In the infinitesimal-strain algorithm, we employ a two-invariant isotropic hyper-elasto-plasticity model based on the modified Cam-Clay model with associative flow rule for the reference unfrozen state [48,55]. We then extend it to capture the mechanical behavior of the frozen state by introducing the cryo-suction effects (cf. [7,16,32]). Presumably, it is possible to extend this framework for the non-associative plasticity models, which may capture the constitutive responses more closely than the associative counterpart. However, in such cases, the restriction imposed by the principle of maximum plastic dissipation must be carefully considered before incorporating non-associative flow rule into the balance of energy equation [56]. This extension is out of the scope of this study, but will be considered in the near future.

Our starting point is to consider the frozen soil as a three-phase porous medium that consists of two constituents that can be viewed as the same two-phase media in two different phase regions (i.e. liquid vs. crystalline solid). An important implication is that one may use the corresponding thermodynamically-consistent Clausius-Clapeyron equation to establish relation among crystal ice pressure  $(p_C)$ , liquid water pressure  $(p_L)$  and temperature (T) [7] at the thermodynamics equilibrium, i.e.,

$$p_{\rm C} = \frac{\rho_{\rm C}}{\rho_{\rm L}} p_{\rm L} - \rho_{\rm C} l \ln \left( \frac{T}{273.15} \right), \tag{29}$$

where the unit of temperature is in Kelvin and l is the specific latent heat of fusion. Notice that, in Eq. (29), the ice pressure is a function of pore water pressure, temperature and the densities of both ice crystal and the unfrozen water. Due to the usage of the exponential/logarithmic mapping, both the ice and pore water pressure described above and the constitutive relation is described in the infinitesimal strain setting. The elastic responses of the frozen soil are replicated by an isotropic hyperelasticity model (cf. [55,57]), with a modification such that the volumetric constitutive law depends on the amount of cryo-suction pressure, i.e.,

$$p' = ks_{\text{cryo}} + (p_0 - ks_{\text{cryo}}) \exp\left(\frac{\varepsilon_{v0} - \varepsilon_v^e}{c_r}\right), \quad q = 3\mu\varepsilon_s^e, \tag{30}$$

where  $p_0$  is the reference pressure;  $s_{\text{cryo}}$  is the cryo-suction given by  $s_{\text{cryo}} = \max(p_{\text{C}} - p_{\text{L}}, 0)$ ; k is the parameter describing the increase in cohesion with suction (cf. [58]);  $\varepsilon_{v0}$  is the reference volumetric strain;  $c_r$  is the elastic compressibility parameter (or recompression index);  $\varepsilon_v^e$  and  $\varepsilon_s^e$  are the volumetric and deviatoric strain invariants of the elastic logarithmic strain, respectively; and  $\mu$  is the elastic shear modulus. Note that the freezing and thawing processes should influence both the stiffness and strength of the three-phase frozen porous media. In this work, our focus is mainly on the latter, following the treatment of Nishimura et al. [7]. Nevertheless, a more comprehensive treatment can be also made by considering that the change of degree of ice saturation affects the elastic stiffness. This can be done via a purely phenomenological approach if sufficient experimental data are available or based on a theoretical approach, such as Eshelby's equivalent inclusion method (e.g., [12,32]). The yield surface of the frozen soil that incorporates the cryo-suction effect is represented as follows,

$$f = \left[p' - \left(\frac{p_c + ks_{\text{cryo}}}{2}\right)\right]^2 + \frac{q^2}{M^2} - \left(\frac{p_c - ks_{\text{cryo}}}{2}\right)^2,\tag{31}$$

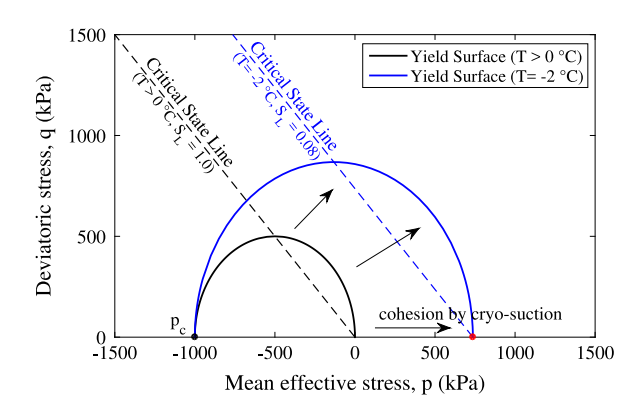


Fig. 1. Change of the yield surface from unfrozen  $(T > 0 \, ^{\circ}\text{C})$  to frozen state  $(T = -2 \, ^{\circ}\text{C})$  – tension is positive.

where  $p_c$  is the preconsolidation stress; M is the slope of critical state line; and p' and q are the mean normal and deviatoric stresses as defined below,

$$p' = \frac{1}{3} \operatorname{tr}(\tau'), \quad q = \sqrt{\frac{3}{2}} \|\xi\|, \quad \xi = \tau' - p'I.$$
 (32)

Fig. 1 indicates how the yield surface and critical state line change from unfrozen to frozen state. We can identify that frozen soil holds stable without the confining pressure due to the apparent cohesion by cryo-suction. We note that the preconsolidation stress ( $p_c$ ) is assumed to be independent upon temperature (cf. [7]).

In the return mapping algorithm for a two-invariant plasticity model, we adopt the hardening law proposed in [48,55,59–61] which takes the following form,

$$\frac{\dot{v}}{v} = -c_c \frac{\dot{p}_c}{p_c},\tag{33}$$

where  $\nu$  is the specific volume of the soil;  $c_c$  is a compressibility index (or compression index). This hardening law allows the hardening parameter  $p_c$  to be expressed exactly as a known function of the plastic volumetric strain  $\varepsilon_v^p$  as,

$$\dot{p}_c = -\frac{\dot{\varepsilon}_v^p}{c_c - c_r} p_c,\tag{34}$$

under the condition of  $0 < c_r < c_c$  [48,55]. Therefore, we employ the residual vector ( $\mathbf{r}$ ) and unknown vector ( $\mathbf{x}$ ) for a local Newton's iteration as follows:

$$\mathbf{r} = \begin{cases} \varepsilon_{v}^{e} - \varepsilon_{v}^{e} & \text{trial} + \Delta \lambda \partial_{p'} f \\ \varepsilon_{s}^{e} - \varepsilon_{s}^{e} & \text{trial} + \Delta \lambda \partial_{q'} f \\ f \end{cases}; \quad \mathbf{x} = \begin{cases} \varepsilon_{v}^{e} \\ \varepsilon_{s}^{e} \\ \Delta \lambda \end{cases}; \quad \mathbf{a} = \mathbf{r}'(\mathbf{x}),$$
(35)

where  $\Delta\lambda$  is the incremental plastic multiplier; f is the yield function in Eq. (31), while  $\partial_{p'}f$  and  $\partial_q f$  indicate the derivative of f with respect to p' and q, respectively; a is the local consistent tangent operator. More details regarding the process of the return mapping algorithm presented herein can be found in [48]. Note that the cryosuction pressure  $(s_{\rm cryo})$  in the local Newton mapping algorithm adopts the global variables of liquid water pressure  $p_{\rm L}$  and temperature T (for  $p_{\rm C}$ ). As the thermal and hydraulic convection–diffusion takes place in the porous media, these two physical quantities are determined not solely from a local material state, but also dependent on the material state of the neighborhood. Through the thermo-hydro-mechanical coupling effect, these non-local effects may affect the path-dependent responses [15]. The physical implications of these nonlocal effects will be further explored through numerical examples in Section 6.

## 3.2. Freezing characteristic function and constitutive law for unfrozen water

In the unsaturated soil mechanics, the water retention curve or the soil-water characteristic function can be derived from the liquid-air interface energy between gas and liquid phases coexisting in the pores. This concept can be

expanded to a three-phase frozen soil in which the frozen soil is idealized as a solid-ice-water mixture. In this case, one relates the difference between the pressure of the ice crystal and the unfrozen water with the degree of saturation of liquid or ice crystal while neglecting the presence of water or vapor in the pores (e.g., [30,31]). The similarity of the soil retention characteristic to the soil moisture characteristic has been studied in a number of previous studies such as [62] and [63]. Assume that pre-melting theory is valid such that thin water film exists in between the ice crystal and solid skeleton, one important mechanism that leads to this similarity is the relative small water-ice interfacial force compared to the water-solid interfacial force. This allows the absorptive forces dominate. Since adsorptive forces only act on the liquid phase, whether ice or air is present at the other side of the water-solid interface does not affect the retention significantly. Consequently, the ice-water interfacial energy can be neglected.

Mimicking the air–water–suction relation in the van Genuchten retention model (cf. [64]) and neglecting the hysteresis due to the dissipation during the freeze–thaw cycles, one may introduce a non-hysteretic phenomenological characteristic function to relate the liquid water saturation with the pressure difference between the crystal ice and the liquid water ( $p_C - p_L > 0$ ), which is cryo-suction [7,32], i.e.,

$$S_{\rm L} = \left[1 + \left(\frac{s_{\rm cryo}}{P}\right)^n\right]^{-m}, \quad s_{\rm cryo} = \max(p_{\rm C} - p_{\rm L}, 0),$$
 (36)

in which P, n and m are material parameters. P is a scaling parameter, and n and m are empirical constants defining the shape of the freezing characteristic curve ( $m = \frac{n-1}{n}$ ). We note that the capillary suction pressure in the water retention curve by van Genuchten [64] for unsaturated soil is replaced by the cryo-suction for saturated frozen soil [7]. We remark that other models for freezing characteristic function can be used (e.g., [31] – using a given value of water content and the porosity; Zhou [32] – a simplified temperature only model). Finally, one may substitute Eq. (29), the Clausius–Clapeyron equation, into Eq. (36) to express the freezing characteristic function of Eq. (36) as a relation among the degree of saturation of liquid water ( $S_L$ ), pore water pressure ( $p_L$ ) and the temperature (T) when  $s_{\rm cryo} > 0$ , that is,

$$S_{L} = \left[ 1 + \left[ \frac{-(1 - \rho_{C}/\rho_{L})p_{L} - \rho_{C}l \ln(T/273.15)}{P} \right]^{n} \right]^{-m}, \tag{37}$$

where the unit of temperature T is Kelvin; l stands for the latent heat of fusion. In the numerical examples shown in Section 6, we adopted the parameter n=2.0, the reference pressure P=200 kPa and the latent heat of fusion l=334 kJ/kg (cf. [7]). The freezing characteristic function becomes a unity when T>0 °C, which leads to unfrozen state fully saturated only with liquid water ( $S_L=1.0$ ). Fig. 2(a) shows how the freezing characteristic function varies by temperature (T) and liquid water pressure ( $p_L$ ). It should be noted that the pore pressure dependence of the freezing characteristic function remains important near the phase transition temperature but exhibits relatively minor impact on the degree of saturation of water once the phase transition completes [7].

The constitutive law for the flow of the unfrozen water is assumed to be Darcian. We adopt the saturation-dependent relative permeability (e.g., [65]) and the temperature-dependent viscosity (e.g., [66]). As a result, for the unfrozen water, the evolution of hydraulic conductivity tensor (k) is formulated using the relation below,

$$\mathbf{k} = \frac{k_r}{\mu_r} \mathbf{k_L},\tag{38}$$

where  $k_r$  and  $\mu_r$  are the relative permeability and the temperature-dependent viscosity, respectively.  $k_L$  is the isotropic hydraulic conductivity tensor at the reference temperature. Meanwhile, the relative permeability and the temperature-dependent viscosity are empirical relations that read,

$$k_r = \sqrt{S_L} \left[ 1 - \left( 1 - S_L^{1/m} \right)^m \right]^2, \quad \mu_r = 1.5963 \times 10^{-2} \exp\left( \frac{509.53}{T - 150} \right).$$
 (39)

Here m is a material parameter described above ( $m = \frac{n-1}{n}$ ), T is the temperature in Kelvin and  $S_L$  is the saturation of liquid water described by freezing characteristic function (e.g., [12,66]). Fig. 2(b) presents how the relative permeability ( $k_r$ ) changes under various liquid water pressure and temperature conditions. The relative permeability is highly sensitive to the change of liquid water pressure and temperature. Nevertheless, the relative permeability and hence the hydraulic conductivity approach to zero once the temperature is lower than approximately -2 °C regardless of the liquid water pressure. Meanwhile, a decrease in temperature will also reduce the viscosity. These two mechanisms make it difficult for the supercooled water to flow as the temperature drops.

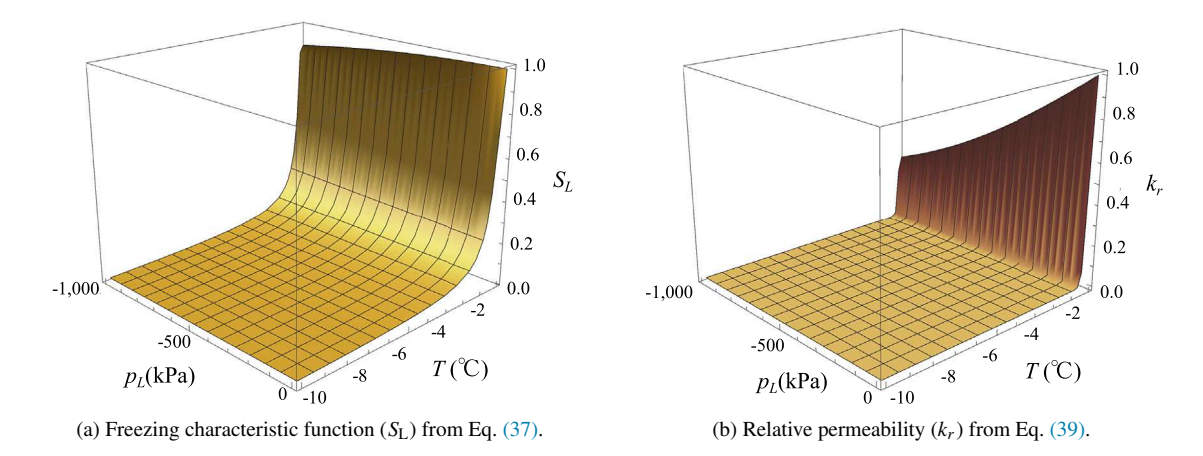


Fig. 2. (a) Freezing characteristic function ( $S_L$ , degree of saturation) and (b) Relative permeability ( $k_r$ ) under different liquid water pressure ( $p_L$ ) and temperature (T) conditions.

#### 4. Variational formulation

In this section, we introduce the variational form, the corresponding equal-order displacement-liquid water pressure—temperature finite element implementation, and the corresponding stabilization procedure of the thermohydro-mechanical model for frozen soil undergoing finite deformation range. We first define the standard weak form of the poromechanics problem based on the conservation laws derived in Section 2. To prevent spurious modes due to the usage of equal order interpolations, we adopt a stabilization mechanism into the weighted-residual statement of the mass and energy balance equations. This will be further discussed in Section 5.1.

#### 4.1. Galerkin form

We proceed the numerical implementation by deriving a weighted residual statement suitable for a total Lagrangian formulation. Firstly, we can consider a reference domain  $\mathcal{B}$  whose boundary  $\partial \mathcal{B}$  is composed of the Dirichlet and von Neumann boundaries as,

$$\partial \mathcal{B} = \overline{\partial \mathcal{B}_{u} \cup \partial \mathcal{B}_{t}} = \overline{\partial \mathcal{B}_{p_{L}} \cup \partial \mathcal{B}_{Q_{p_{t}}}} = \overline{\partial \mathcal{B}_{T} \cup \partial \mathcal{B}_{Q_{T}}}, \tag{40}$$

$$\emptyset = \overline{\partial \mathcal{B}_{\boldsymbol{u}} \cap \partial \mathcal{B}_{\boldsymbol{t}}} = \overline{\partial \mathcal{B}_{p_{L}} \cap \partial \mathcal{B}_{\mathcal{Q}_{p_{L}}}} = \overline{\partial \mathcal{B}_{T} \cap \partial \mathcal{B}_{\mathcal{Q}_{T}}}, \tag{41}$$

where  $\partial \mathcal{B}_{u}$  is the solid displacement boundary;  $\partial \mathcal{B}_{t}$  is the solid traction boundary;  $\partial \mathcal{B}_{p_{L}}$  is the liquid water pressure boundary;  $\partial \mathcal{B}_{Q_{p_{L}}}$  is the liquid water fluid flux boundary;  $\partial \mathcal{B}_{T}$  is the temperature boundary;  $\partial \mathcal{B}_{Q_{T}}$  is the heat flux boundary. Dirichlet boundary conditions of the thermo-hydro-mechanical (THM) problem for frozen soil read,

$$\begin{cases}
 u = \overline{u} \text{ on } \partial \mathcal{B}_{u}, \\
 p_{L} = \overline{p_{L}} \text{ on } \partial \mathcal{B}_{p_{L}}, \\
 T = \overline{T} \text{ on } \partial \mathcal{B}_{T}.
\end{cases}$$
(42)

Meanwhile, the von Neumann boundary conditions that describe the traction and fluxes read,

$$\begin{cases}
P \cdot N = \overline{t} \text{ on } \partial \mathcal{B}_{t}, \\
-N \cdot Q_{p_{L}} = \overline{Q}_{p_{L}} \text{ on } \partial \mathcal{B}_{Q_{p_{L}}}, \\
-N \cdot Q_{T} = \overline{Q}_{T} \text{ on } \partial \mathcal{B}_{Q_{T}},
\end{cases} (43)$$

where N is the outward normal vector on the reference configuration  $\partial \mathcal{B}$ . In addition, we consider the trial space for the weak form that reads.

$$V_{\boldsymbol{u}} = \left\{ \boldsymbol{u} : \mathcal{B} \to \mathbb{R}^3 | \boldsymbol{u} \in [H^1(\mathcal{B})]^3, \ \boldsymbol{u}|_{\partial \mathcal{B}_{\boldsymbol{u}}} = \overline{\boldsymbol{u}} \right\},\tag{44}$$

$$V_{p_{L}} = \left\{ p_{L} : \mathcal{B} \to \mathbb{R} | p_{L} \in H^{1}(\mathcal{B}), \ p_{L}|_{\partial \mathcal{B}_{p_{L}}} = \overline{p_{L}} \right\}, \tag{45}$$

$$V_T = \left\{ T : \mathcal{B} \to \mathbb{R} | T \in H^1(\mathcal{B}), \ T|_{\partial \mathcal{B}_T} = \overline{T} \right\}. \tag{46}$$

Here,  $H^1$  denotes the Sobolev space of degree one. The admissible variations of the displacement  $\eta$ , liquid water pressure  $\psi$  and temperature  $\theta$  read,

$$V_{\eta} = \left\{ \boldsymbol{\eta} : \mathcal{B} \to \mathbb{R}^3 | \boldsymbol{\eta} \in [H^1(\mathcal{B})]^3, \ \boldsymbol{\eta}|_{\partial \mathcal{B}_{\boldsymbol{u}}} = \boldsymbol{0} \right\},\tag{47}$$

$$V_{\psi} = \left\{ \psi : \mathcal{B} \to \mathbb{R} | \psi \in H^{1}(\mathcal{B}), \ \psi|_{\partial \mathcal{B}_{p_{L}}} = 0 \right\}, \tag{48}$$

$$V_{\theta} = \left\{ \theta : \mathcal{B} \to \mathbb{R} | \theta \in H^{1}(\mathcal{B}), \ \theta |_{\partial \mathcal{B}_{T}} = 0 \right\}. \tag{49}$$

Therefore, the weighted residual statement of the balance of linear momentum, mass and energy are: find  $u \in V_u$ ,  $p_L \in V_{p_L}$  and  $T \in V_T$  such that for all  $\eta \in V_{\eta}$ ,  $\psi \in V_{\psi}$  and  $\theta \in V_{\theta}$ ,

$$G(\mathbf{u}, p_{L}, T, \eta) = H(\mathbf{u}, p_{L}, T, \psi) = L(\mathbf{u}, p_{L}, T, \theta) = 0,$$
 (50)

where  $G: V_u \times V_{p_L} \times V_T \times V_{\eta} \to \mathbb{R}$  is the weak statement of the balance of linear momentum, that is,

$$G(\boldsymbol{u}, p_{L}, T, \boldsymbol{\eta}) = \int_{\mathcal{B}} \left[ \nabla^{X} \boldsymbol{\eta} : \boldsymbol{P} - J \rho \boldsymbol{\eta} \cdot \boldsymbol{G} \right] dV - \int_{\partial \mathcal{B}_{t}} \boldsymbol{\eta} \cdot \bar{\boldsymbol{t}} d\Gamma.$$
 (51)

 $H: V_{\mathbf{u}} \times V_{p_{\mathrm{L}}} \times V_{T} \times V_{\psi} \to \mathbb{R}$  is the weak statement of the balance of mass, that is,

$$H(\boldsymbol{u}, p_{L}, T, \psi) = \int_{\mathcal{B}} \psi \left[ (1 - \phi^{S})(\rho_{L} - \rho_{C}) \dot{S}_{L} \right] J dV + \int_{\mathcal{B}} \psi \left[ \rho_{L} S_{L} + \rho_{C} (1 - S_{L}) \right] \dot{J} dV - \int_{\mathcal{B}} \nabla^{X} \psi \cdot \boldsymbol{W} dV - \int_{\partial \mathcal{B}_{Q_{R}}} \psi \overline{Q}_{p} d\Gamma.$$
(52)

And  $L: V_{\mathbf{u}} \times V_{p_1} \times V_T \times V_{\theta} \to \mathbb{R}$  is the weak statement of the balance of energy, that is,

$$L(\mathbf{u}, p_{L}, T, \theta) = \int_{\mathcal{B}} \theta \left(Jc_{F}\right) \dot{T} dV + \int_{\mathcal{B}} \nabla^{X} \theta \cdot \mathbf{K}_{T} \cdot \nabla^{X} T dV - \int_{\mathcal{B}} \theta \left(\frac{\phi^{L} S_{L} c_{FL}}{\rho_{L}} \mathbf{W} \cdot \mathbf{F}^{-T} \cdot \nabla^{X} T\right) dV - \int_{\partial \mathcal{B}_{Q_{T}}} \theta \overline{Q}_{T} d\Gamma.$$

$$(53)$$

## 4.2. Consistent linearization

Since we use an implicit time integration scheme to solve the system of equations, it is essential to either approximate or obtain the exact expression of the consistent tangent such that the solution fields of u,  $p_L$  and T can be updated in an incremental fashion. Here we perform the consistent linearization of the weak form (51)–(53) with respect to variation of displacement, pore pressure and temperature. We first focus on the linearization of momentum balance equation which adopts the infinitesimal strain algorithm including the pre and post–processing steps. This can be represented as:

$$\delta G(\boldsymbol{u}, p_{L}, T, \boldsymbol{\eta}) = \int_{\mathcal{B}} \nabla^{X} \boldsymbol{\eta} : \boldsymbol{A} : \delta \boldsymbol{F} dV - \int_{\mathcal{B}} \nabla^{X} \boldsymbol{\eta} : \delta (J \boldsymbol{F}^{-T} \bar{p}) dV$$

$$- \int_{\mathcal{B}} \boldsymbol{\eta} \cdot \delta (J \rho \boldsymbol{G}) - \int_{\partial \mathcal{B}_{t}} \boldsymbol{\eta} \cdot \delta \bar{t} d\Gamma = 0,$$
(54)

where A in the first term is defined as in Eq. (55). The partial derivative of the effective first Piola–Kirchhoff stress with respect to the deformation gradient or other tangential stiffness tensor stemmed from other energy-conjugate pair

must be sought, that is,

$$A \equiv \frac{\partial \mathbf{P}'}{\partial \mathbf{F}}, \quad \mathbf{P}' = J\mathbf{\sigma}' \cdot \mathbf{F}^{-T} = \mathbf{\tau}' \cdot \mathbf{F}^{-T}. \tag{55}$$

Expressing A in terms of index notation using the effective Kirchhoff stress  $\tau'$  and considering two point tensors F and P' yield,

$$A_{iMkN} = \frac{\partial P'_{iM}}{\partial F_{kN}} = \frac{\partial \tau'_{ip}}{\partial F_{kN}} F_{Mp}^{-1} + \tau'_{ip} \frac{\partial F_{Mp}^{-1}}{\partial F_{kN}}.$$
(56)

Note that the difference of  $F^{-1}$  and  $F^{-T}$  should be considered in tensor and index notations,

$$\boldsymbol{F}^{-1} = F_{Ji}^{-1} \boldsymbol{G}_J \otimes \boldsymbol{g}_i, \quad \boldsymbol{F}^{-T} = F_{Ji}^{-1} \boldsymbol{g}_i \otimes \boldsymbol{G}_J, \tag{57}$$

where  $g_i$  and  $G_J$  stand for the basis vectors of current and reference configurations, respectively. A logarithmic/exponential mapping is employed to allow infinitesimal strain constitutive law extended into the geometrical nonlinear regime [35,53]. As a result, the Kirchhoff stress in the first term of Eq. (56) can be updated by means of the incremental constitutive function of small strain algorithm ( $\tilde{\tau}$ )

$$\frac{\partial \boldsymbol{\tau}'}{\partial \boldsymbol{F}} = \frac{\partial \tilde{\boldsymbol{\tau}}}{\partial \boldsymbol{\epsilon}^e \text{ trial}} : \frac{\partial \boldsymbol{\epsilon}^e \text{ trial}}{\partial \boldsymbol{B}^e \text{ trial}} : \frac{\partial \boldsymbol{B}^e \text{ trial}}{\partial \boldsymbol{F}}, \tag{58}$$

where,

$$\frac{\partial \hat{\tau}}{\partial \epsilon^{e \text{ trial}}} = D = \text{ infinitesimal-strain elastoplastic consistent tangent operator,}$$
 (59)

$$\frac{\partial \boldsymbol{\epsilon}^{e \text{ trial}}}{\partial \boldsymbol{B}^{e \text{ trial}}} = \mathbf{L} = \frac{\partial \ln \boldsymbol{B}^{e \text{ trial}}}{\partial \boldsymbol{B}^{e \text{ trial}}},\tag{60}$$

$$\frac{\partial \mathbf{B}^{e \text{ trial}}}{\partial \mathbf{F}} = \mathbf{B}, \quad \mathbf{B}_{ipkN} = \delta_{ik} (\mathbf{F}^{e \text{ trial}})_{pN} + \delta_{pk} (\mathbf{F}^{e \text{ trial}})_{iN}, \tag{61}$$

by the definition of the left Cauchy–Green tensor **B**.

As stated D can be obtained from the infinitesimal-strain constitutive model in Section 3.1. More details regarding the process of deriving the consistent tangent operator D can be found in [48]. In the second term of Eq. (56), the tensor derivative of the inverse of deformation gradient can be derived using the derivative of the second order identity tensor, which gives:

$$\frac{\partial F_{Mp}^{-1}}{\partial F_{kN}} = -F_{Ml}^{-1} \delta_{lk} \delta_{MN} F_{Mp}^{-1} = -F_{Mk}^{-1} F_{Np}^{-1}. \tag{62}$$

Note that the linearization for update of the effective first Piola–Kirchhoff stress (P') in Eq. (55) includes not only the consistent tangent operator from the infinitesimal-strain constitutive model (Eq. (59)) but other terms as in Eqs. (56)–(62) to be represented in the total Lagrangian framework considering the geometrical nonlinearity at finite deformation regime. As stated, the associative flow rule is used and the general elastic predictor/return-mapping algorithm is adopted through the relationship between the Kirchhoff stress ( $\tau'$ ) and the elastic logarithmic strain ( $\varepsilon = \frac{1}{2} \ln B$ ), from the left Cauchy–Green tensor B. Note again that this relation requires the exact calculation of derivative of logarithmic tensor or consideration of higher order terms in Taylor expansion while deriving the consistent tangent stiffness matrix. The following relations can be used for linearization [38]:

$$\delta \mathbf{F} = \nabla^{\mathbf{X}} (\delta \mathbf{u}), \quad \delta \mathbf{F}^{-1} = -\mathbf{F} \cdot \nabla^{\mathbf{X}} (\delta \mathbf{u}), \quad \delta J = J \nabla^{\mathbf{X}} \cdot (\delta \mathbf{u}), \tag{63}$$

where we recall the following identities [67,68]:  $\nabla^x(\delta u) = \nabla^X(\delta u) \cdot F^{-1}$  and  $\nabla^x \cdot (\delta u) = \nabla^X(\delta u) : F^{-T}$ . Next the linearization of the mass balance equation reads:

$$\delta H(\boldsymbol{u}, p_{L}, T, \psi) = \delta \left( \int_{\mathcal{B}} \psi \left[ (1 - \phi^{S})(\rho_{L} - \rho_{C}) \dot{S}_{L} \right] J dV \right) + \delta \left( \int_{\mathcal{B}} \psi \left[ \rho_{L} S_{L} + \rho_{C} (1 - S_{L}) \right] \dot{J} dV \right) - \int_{\mathcal{B}} \nabla^{X} \psi \cdot \delta \boldsymbol{W} dV - \int_{\partial \mathcal{B}_{Q_{p}}} \psi \delta \overline{Q}_{p} d\Gamma,$$

$$(64)$$

where the linearization of  $S_L$  can be conducted by considering a function of  $p_L$  and T as in Eq. (37). In addition, we can use the relation  $\dot{J} = J \nabla^x \cdot \dot{u}$  and  $\nabla^x \cdot \dot{u} = \nabla^X \dot{u} : F^{-T}$  [68]. The linearization of the Lagrangian relative liquid water mass flux, W, requires the linearization of the pull-back permeability tensor  $K_L$ , which is represented based on  $K_L$  in Eq. (38), that is,

$$\delta \mathbf{K}_{L} = \delta \left( J \mathbf{F}^{-1} \cdot \mathbf{k} \cdot \mathbf{F}^{-T} \right) = \delta \left( J \right) \mathbf{F}^{-1} \cdot \mathbf{k} \cdot \mathbf{F}^{-T} + J \delta \left( \mathbf{F}^{-1} \right) \cdot \mathbf{k} \cdot \mathbf{F}^{-T}$$

$$+ J \mathbf{F}^{-1} \cdot \delta \left( \mathbf{k} \right) \cdot \mathbf{F}^{-T} + J \mathbf{F}^{-1} \cdot \mathbf{k} \cdot \delta \left( \mathbf{F}^{-T} \right),$$

$$\text{with } \delta(\mathbf{k}) = \frac{\partial \mathbf{k}}{\partial k_{r}} \delta k_{r} + \frac{\partial \mathbf{k}}{\partial \mu_{r}} \delta \mu_{r} = \frac{\mathbf{k}_{L}}{\mu_{r}} \frac{\partial k_{r}}{\partial S_{L}} \delta S_{L} + \left( -\frac{k_{r}}{\mu_{r}^{2}} \mathbf{k}_{L} \right) \frac{\partial \mu_{r}}{\partial T} \delta T$$

$$= \frac{\mathbf{k}_{L}}{\mu_{r}} \frac{\partial k_{r}}{\partial S_{L}} \frac{\partial S_{L}}{\partial p_{L}} \delta p_{L} + \left[ \frac{\mathbf{k}_{L}}{\mu_{r}} \frac{\partial k_{r}}{\partial S_{L}} \frac{\partial S_{L}}{\partial T} + \left( -\frac{k_{r}}{\mu_{r}^{2}} \mathbf{k}_{L} \right) \frac{\partial \mu_{r}}{\partial T} \right] \delta T.$$

$$(65)$$

Finally the linearization of energy balance equation can be performed as the same procedure for momentum and mass balance equations, that is,

$$\delta L\left(\boldsymbol{u}, p_{L}, T, \theta\right) = \int_{\mathcal{B}} \theta \delta \left(J c_{F} \dot{T}\right) dV + \int_{\mathcal{B}} \nabla^{X} \theta \cdot \delta \left(\boldsymbol{K}_{T} \cdot \nabla^{X} T\right) dV - \int_{\mathcal{B}} \theta \delta \left(\frac{\phi^{L} S_{L} c_{FL}}{\rho_{L}} \boldsymbol{W} \cdot \boldsymbol{F}^{-T} \cdot \nabla^{X} T\right) dV - \int_{\partial \mathcal{B}_{Q_{T}}} \theta \delta \overline{Q}_{T} d\Gamma.$$

$$(67)$$

Note that the linearization of  $K_T$  can be sought considering Eqs. (25) and (27) following the procedure for the pull-back permeability tensor in Eq. (65).

#### 4.3. Time discretization

In order to solve the transient boundary value problem, the weak statement in Eq. (50) is discretized in time. In this implementation, the solution is incrementally advanced via the backward Euler scheme following [14,37]. The time-discretized weighted-residual form reads,

$$\hat{G}(\mathbf{u}_{n+1}, p_{Ln+1}, T_{n+1}, \mathbf{\eta}) = \hat{H}(\mathbf{u}_{n+1}, p_{Ln+1}, T_{n+1}, \psi) = \hat{L}(\mathbf{u}_{n+1}, p_{Ln+1}, T_{n+1}, \theta) = 0,$$
(68)

where the discrete weak form of the balance of linear momentum now reads

$$G\left(\boldsymbol{u}_{n+1}, p_{Ln+1}, T_{n+1}, \boldsymbol{\eta}\right) = \int_{\mathcal{B}} \left[ \nabla^{X} \boldsymbol{\eta} : \boldsymbol{P}_{n+1} - \left(J_{n+1} \rho_{n+1}\right) \boldsymbol{\eta} \cdot \boldsymbol{G} \right] dV - \int_{\partial \mathcal{B}_{t}} \boldsymbol{\eta} \cdot \bar{\boldsymbol{t}}_{n+1} d\Gamma.$$

$$(69)$$

Similarly, the discrete weak form of the mass and energy balance equations can be represented as

$$H\left(\boldsymbol{u}_{n+1}, p_{Ln+1}, T_{n+1}, \psi\right) = \int_{\mathcal{B}} \psi \left[ (1 - \phi_{n+1}^{S})(\rho_{L} - \rho_{C}) \frac{(S_{L})_{n+1} - (S_{L})_{n}}{\Delta t} \right] J_{n+1} dV$$

$$+ \int_{\mathcal{B}} \psi \left[ \rho_{L} S_{L} + \rho_{C} (1 - S_{L}) \right]_{n+1} J_{n+1} \frac{\nabla^{X} \left(\boldsymbol{u}_{n+1} - \boldsymbol{u}_{n}\right)}{\Delta t} : \boldsymbol{F}_{n+1}^{-T} dV$$

$$- \int_{\mathcal{B}} \nabla^{X} \psi \cdot \boldsymbol{W}_{n+1} dV - \int_{\partial \mathcal{B}_{Qp}} \psi \overline{Q}_{p_{n+1}} d\Gamma, \qquad (70)$$

$$L\left(\boldsymbol{u}_{n+1}, p_{Ln+1}, T_{n+1}, \theta\right) = \int_{\mathcal{B}} \theta \left(J_{n+1} c_{Fn+1}\right) \frac{T_{n+1} - T_{n}}{\Delta t} dV + \int_{\mathcal{B}} \nabla^{X} \theta \cdot \boldsymbol{K}_{Tn+1} \cdot \nabla^{X} T_{n+1} dV$$

$$- \int_{\mathcal{B}} \theta \left[ \left(\frac{\phi^{L} S_{L} c_{FL}}{\rho_{L}}\right)_{n+1} \boldsymbol{W}_{n+1} \cdot \boldsymbol{F}_{n+1}^{-T} \cdot \nabla^{X} T_{n+1} \right] dV - \int_{\partial \mathcal{B}_{Qr}} \theta \overline{Q}_{T_{n+1}} d\Gamma. \qquad (71)$$

## 4.4. Spatial discretization

In this study, we introduce the standard shape functions of equal-order interpolation (linear) to the testing functions and field variables. Therefore, the following approximations are adopted:

$$\begin{cases} \boldsymbol{u} \approx \boldsymbol{u}^{h} = \sum_{a=1}^{n} N_{a} \boldsymbol{u}_{a}, \\ p_{L} \approx p_{L}^{h} = \sum_{a=1}^{n} N_{a} p_{La}, \\ T \approx T^{h} = \sum_{a=1}^{n} N_{a} T_{a}, \end{cases} \begin{cases} \boldsymbol{\eta} \approx \boldsymbol{\eta}^{h} = \sum_{a=1}^{n} N_{a} \boldsymbol{\eta}_{a}, \\ \boldsymbol{\psi} \approx \boldsymbol{\psi}^{h} = \sum_{a=1}^{n} N_{a} \boldsymbol{\psi}_{a}, \\ \boldsymbol{\theta} \approx \boldsymbol{\theta}^{h} = \sum_{a=1}^{n} N_{a} \boldsymbol{\theta}_{a}. \end{cases}$$
(72)

Here the superscript h indicates a spatially discretized function;  $N_a$  is the shape function matrix;  $u_a$ ,  $p_{La}$  and  $T_a$  are the nodal values of displacement, liquid water pressure, and temperature;  $\eta_a$ ,  $\psi_a$  and  $\theta_a$  denote the nodal values of corresponding test functions; n indicates the number of node per element. We can substitute the approximations of Eq. (72) into Eq. (68) and take  $\hat{G}$ ,  $\hat{H}$  and  $\hat{L}$  as residuals of the full discrete system of equations for THM problems. This leads to three-field mixed finite element formulations of the thermo-hydro-mechanical model for frozen soil in which the Jacobian system in each Newton update has a following form:

$$\begin{bmatrix} \mathbf{A} & \mathbf{B}_1 & \mathbf{D}_1 \\ \mathbf{B}_2 & \mathbf{C} & \mathbf{E}_1 \\ \mathbf{D}_2 & \mathbf{E}_2 & \mathbf{F} \end{bmatrix} \begin{bmatrix} \delta \boldsymbol{u} \\ \delta \boldsymbol{p}_L \\ \delta \boldsymbol{T} \end{bmatrix} = - \begin{bmatrix} \mathbf{R}_{\text{mom.}} \\ \mathbf{R}_{\text{mas.}} \\ \mathbf{R}_{\text{ene.}} \end{bmatrix}.$$
(73)

Note that the Jacobian has a three by three block structure;  $\delta u$ ,  $\delta p_{\rm L}$ ,  $\delta T$  are the nodal incrementals over given time interval for displacement, liquid water pressure and temperature fields;  $\mathbf{R}_{\rm mom.}$ ,  $\mathbf{R}_{\rm mas.}$ ,  $\mathbf{R}_{\rm ene.}$  are residuals of the balance of linear momentum, mass and energy as in Eqs. (68)–(71). A detailed expression of 3  $\times$  3 Jacobian is listed in Appendix.

## 5. Highlights of numerical issues and the responding remedy

This section describes two numerical issues raised from the THM system for frozen soil, namely, (1) the lack of two-fold inf-sup condition and (2) a system of equation with high condition number and proposed possible solutions to overcome them. The issue of the lack of two-fold inf-sup condition is caused by the usage of equal-order finite dimensional space for displacement, liquid water pressure and temperature. This well-known effect has been intensively studied for poromechanics problems in the last few decades (e.g., [11,14,37,69–71]). Here, we adopt the stabilization procedure to overcome this numerical deficiency. To ensure that the stabilization procedure we used leads to stable results, we introduce a new numerical test called weak two-fold inf-sup tests to check whether solution remains stable for arbitrary mesh size. Furthermore, we have also exploited ways to introduce a pre-conditioner specialized for the THM system to speed up the simulations.

## 5.1. Spatial stability and two-fold inf-sup tests

In classical poromechanics FEM models that employ solid displacement and pore pressure as the prime variables, the interpolated pore pressure field is known to suffer from spurious oscillation in the undrained limit (e.g., [19,72]) if displacement and pore pressure are spanned by the same basis function. The cause of the problem is due to the lack of inf–sup condition (e.g., [19,37,73]). Similar spurious oscillations have been addressed in THM problem with the equal-order finite element when the prime variables of the displacement, pore pressure and temperature were considered in a very fine temporal discretization or near the undrained limit [14,74]. Previously, Liu et al. [74] introduced an interior-penalty procedure on the discrete Galerkin model of the thermo-hydro-mechanics problem in geometrically nonlinear range. On the other hand, Sun [14] analyses the cause of the spurious oscillation of pore pressure and temperature and proposes a projection-based stabilization method for the finite-strain thermo-hydro-mechanical problem to eliminate the spurious modes in the pore pressure and temperature [75]. In this study, we adopt the polynomial projection scheme of Sun [14] to stabilize the THM problems, in which the inf–sup deficiency of equal-order finite element is counterbalanced using stabilization terms based on the weak two-fold inf–sup condition. Nevertheless, a systematical numerical procedure to test the validity of the stabilization procedure has not yet proposed.

Our starting point is the result from [76] which proves that saddle-point problems containing more than two solution fields require the two-fold inf–sup condition to maintain spatial stability (e.g., [14,71]). By considering the finite

element model with a saddle point structure form:  $(\boldsymbol{u}^h, p_L^h, T^h) \in \boldsymbol{V}_{\boldsymbol{u}}^h \times V_{p_L}^h \times V_T^h$ , where  $\boldsymbol{V}_{\boldsymbol{u}}^h, V_{p_L}^h$  and  $V_T^h$  are the finite dimensional spaces chosen for displacement, liquid water pressure and temperature interpolations, the discrete two-fold inf–sup condition holds if and only if there exists a constant  $C_0 > 0$  such that,

$$\sup_{\mathbf{w}^{h} \in V_{L}^{h}} \frac{\int_{\mathcal{B}} \left( ap_{L}^{h} + bT^{h} \right) \nabla^{x} \cdot \mathbf{w}^{h} dV}{\|\mathbf{w}^{h}\|_{V_{L}^{h}}} \ge C_{0} \left( \|p_{L}^{h}\|_{V_{p_{L}}^{h}} + \|T^{h}\|_{V_{T}^{h}} \right) \quad \text{where, } (p_{L}^{h}, T^{h}) \in V_{p_{L}}^{h} \times V_{T}^{h}. \tag{74}$$

Note that the coefficients of a and b are described by  $S_L$ ,  $S_C (=1-S_L)$  and  $p_C$  which are functions of liquid water pressure and temperature fields (i.e.,  $a = \partial(S_L p_L)/\partial p_L + \partial(S_C p_C)/\partial p_L$ ,  $b = \partial(S_L p_L/\partial T) + \partial(S_C p_C)/\partial T)$ ;  $\|\cdot\|_{V_{p_L}^h}$  and  $\|\cdot\|_{V_{p_L}^h}$  are the norms corresponding to the finite dimensional space  $V_u^h$ ,  $V_{p_L}^h$  and  $V_T^h$ . The same associated norms are equipped to the solution spaces and their corresponding test functions. We choose the norm  $\|\cdot\|_{V_u^h} = \|\cdot\|_1$  and  $\|\cdot\|_{V_{p_L}^h} = \|\cdot\|_{V_p^h} = \|\cdot\|_0$ , where  $\|\cdot\|_k$  indicates the standard Sobolev norm of order k, which leads to the relation,  $C_0 \left(\|p_L^h\|_{V_{p_L}^h} + \|T^h\|_{V_p^h}\right) \ge C_0 \left(\|p_L^h + T^h\|_0\right)$ . Adopting the same basis functions for displacement, liquid pore pressure and temperature leads to a formulation that lacks the two-fold inf–sup condition as stated in Eq. (74). However, as pointed out in [14], the spurious pressure and temperature oscillations due to the lack of two-fold inf–sup condition can be eliminated by introducing the additional gradient or projection terms that counterbalance the inf–sup deficiency. This study adopted the projection stabilization scheme to eliminate the spurious oscillations. Note that an analytical proof of the inf–sup condition for a particular choice of finite dimensional spaces can be difficult [77]. As an alternative, we introduce the numerical inf–sup test (e.g., [70,77–81]) for analyzing the thermo-hydro-mechanical formulation. The underlying idea of this inf–sup test is to consider the liquid water pressure and temperature fields together as a product space and introduce proper norms for this product space. Following this step, one may solve a series of generalized eigenvalue problems of Eq. (75) corresponding to the inf–sup condition (cf. Eq. (74)) for a selected number of elements, that is,

$$\mathbf{G}^h \mathbf{V}^h = \lambda \mathbf{S}^h \mathbf{V}^h,\tag{75}$$

where  $\lambda_p$  is the smallest non-zero eigenvalue, in which  $\sqrt{\lambda_p}$  corresponds to the inf–sup value; the matrices  $\mathbf{G}^h$  and  $\mathbf{S}^h$  are defined for a given finite element discretization, as detailed in Refs. [77] and [78]. To perform a two-fold inf–sup test for the product space, one may partition the Jacobian matrix of Eq. (73) such that,

$$\begin{bmatrix} \mathbf{A} & \mathbf{B}_1 & \mathbf{D}_1 \\ \mathbf{B}_2 & \mathbf{C} & \mathbf{E}_1 \\ \mathbf{D}_2 & \mathbf{E}_2 & \mathbf{F} \end{bmatrix} \rightarrow \begin{bmatrix} \mathbf{A} & \mathbf{H}_1 \\ \mathbf{H}_2 & \mathbf{K} \end{bmatrix}, \text{ where } \mathbf{H}_1 = \begin{bmatrix} \mathbf{B}_1 & \mathbf{D}_1 \end{bmatrix}, \mathbf{H}_2 = \begin{bmatrix} \mathbf{B}_2 \\ \mathbf{D}_2 \end{bmatrix}, \text{ and } \mathbf{K} = \begin{bmatrix} \mathbf{C} & \mathbf{E}_1 \\ \mathbf{E}_2 & \mathbf{F} \end{bmatrix}.$$
 (76)

We limit our focus in a very fine temporal discretization in which the heat transfer and pore-fluid diffusion terms are both assumed to be minor. Note that this limit case leads the matrices  $\mathbf{H}_1$  and  $\mathbf{H}_2$  to be  $\mathbf{H}_1 \approx \mathbf{H}_2^T = \mathbf{H}$  (cf. Eq. (A.84) and [71]).

Following [78] and [79] and two-fold inf–sup test of Howell and Walkington [76] and Sun and Mota [81] based on Eqs. (74) and (76), the matrices for the eigenvalue problem in Eq. (75) are represented as,

$$\mathbf{G}^h = \mathbf{H}^h \mathbf{K}^h (\mathbf{H}^h)^{\mathrm{T}} \quad \text{and} \quad (\mathbf{w}^h)^{\mathrm{T}} \mathbf{S}^h \mathbf{w}^h = \|\mathbf{w}^h\|_{V_n^h}^2, \tag{77}$$

where  $\mathbf{H}^h$  and  $\mathbf{K}^h$  are the expressions of  $\mathbf{H}$  and  $\mathbf{K}$  discretized by shape functions (cf. Eq. (72)). Meanwhile, the expression of  $\mathbf{G}^h$  depends on the choice of weighted norm equipped for the product space of the interpolated pore pressure and temperature. In our case, we follow the procedures depicted in [79,82,83] and simply use the condensed lower diagonal matrix  $\mathbf{K}^h$  to form the weighted norms. It should be noted that this particular  $\mathbf{G}^h$  is not the only valid choice. For instance, one may also replace  $\mathbf{K}^h$  with its inverse in Eq. (77) such that the two-fold inf–sup test is directly related to the statically condensed system of equations as have done in [81]. However, as pointed out in [78], a choice that involves inversed matrix may likely increase the computational cost for evaluating the inf–sup tests due to the fact that the inverse matrix is more dense and the inverse operation can also be costly.  $\mathbf{S}^h$ , which is referred as the norm matrix in [78], is obtained from the linear operator that gives the norm  $\|\cdot\|_{V_u^h}$  following [77], in which  $\|\mathbf{u}^h\|_1^2 = \int_{\mathcal{B}} \nabla^x \mathbf{u} \cdot \nabla^x \mathbf{u} dV$  (cf. [14,70,84]). Note that the numerical inf–sup value is sensitive to the norms chosen to construct the inf–sup test. While the existence of the inf–sup value and hence the validity of the inf–sup condition can be proved by any equivalent norms, the actual choice of the norms used to construct the inf–sup test may affect the trend of the numerical inf–sup values upon mesh refinement [80,82]. Here we select the problem of 1D thawing

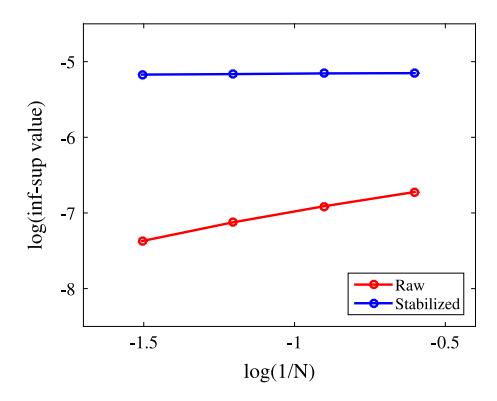


Fig. 3. Inf-sup test of 1D thawing consolidation (the results from the number of elements with 4, 8, 16 and 32 are presented).

consolidation for the numerical inf–sup test. The problem description including boundary conditions can be found in Section 6.1. The number of elements with 4, 8, 16 and 32 are selected for the numerical inf–sup test (Fig. 3). The stabilized inf–sup value is bounded which indicates the test is passed (e.g., [70,77,79,80]).

## 5.2. Pre-conditioner

It is well acknowledged that the implicit monolithic solvers for mixed finite element may lead to ill-conditioning tangential matrix system [85,86]. Since the residuals of the balance of mass, linear momentum and energy are all of different units, the eigenvalues and singular values of the block matrix system could be of several orders of difference and in different signs. Presumably, direct solvers such as Gaussian elimination may allow one to obtain incremental updates even when condition number of the tangent is high, provided that the condition number is still sufficiently small compared with the inverse of the machine error. Nevertheless, the direct solvers are often slower due to the significantly higher numbers of arithmetic operations required. Another feasible possibility to resolve this issue is to design a proper pre-conditioner and then use it with an iterative solver. This approach is adopted in this study. The implementation of the preconditioner leverages the open source finite element library, deal.II (cf. [87,88]) interfaced with p4est mesh handling library [89], and algorithm libraries from the Trilinos project [90]. When the coupled thermo-hydro-mechanical (THM) model is solved in an implicit monolithic scheme, the nonlinear system of equations may lead to a three-by-three block-partitioned tangential matrix through a consistent linearization process (Section 4.2). In this study, we extended the block-preconditioned Newton–Krylov solvers for originally designed for a u/p formulation by Dawson et al. [91] and White and Borja [85]. The underlying idea is to simply consider the space of the interpolated pore pressure and temperature fields as a product space and design a pre-conditioner such that.

$$\mathbf{P}^{-1}\mathbf{J}x = \mathbf{P}^{-1}b,\tag{78}$$

where **J** is the Jacobian;  $\mathbf{x}$  is the solution fields;  $\mathbf{b}$  is the residuals;  $\mathbf{P}^{-1}$  is the preconditioner. The strategy of preconditioning is to choose  $\mathbf{P} \approx \mathbf{L}$  such that  $\mathbf{P}^{-1}\mathbf{J} \approx \mathbf{U}$  when a block LU factorization of **J** is concerned as  $\mathbf{J} = \mathbf{L}\mathbf{U}$ , in which the quality of this approximation determines how fast the Krylov solver converges [85]. In this study, we first express the 3 by 3 system of equations (Eq. (73)) into 2 by 2 system as written in Eq. (76). In this case, the block Schur complement with respect to  $\mathbf{A}$  is  $\mathbf{S} = \mathbf{K} - \mathbf{H}_2 \mathbf{A}^{-1} \mathbf{H}_1$  (cf. [92]). Therefore, the template using the "exact" preconditioner and its approximation can be described as,

$$\mathbf{P}^{-1} = \begin{bmatrix} \mathbf{A}^{-1} & \mathbf{0} \\ \mathbf{S}^{-1} \mathbf{H}_2 \mathbf{A}^{-1} & \mathbf{S}^{-1} \end{bmatrix} \approx \begin{bmatrix} \mathbf{P}_{\mathbf{A}}^{-1} & \mathbf{0} \\ \mathbf{P}_{\mathbf{S}}^{-1} \mathbf{H}_2 \mathbf{P}_{\mathbf{A}}^{-1} & \mathbf{P}_{\mathbf{S}}^{-1} \end{bmatrix}.$$
(79)

Note that the exact inverses  $A^{-1}$  and  $S^{-1}$  are too expensive to compute, which requires designing good approximations  $(\mathbf{P}_{\mathbf{A}}^{-1})$  and  $\mathbf{P}_{\mathbf{S}}^{-1}$ . In particular, we extend the approximation of Schur complement (S) for THM problem based on the

**Table 1**Residence norm (square root of the inner product of residual column vector) and the number of Krylov iterations at the selected Newton steps for comparison of preconditioning strategy (coarse mesh condition with the total degrees of freedom 120).

Newton steps	No preconditioning		Diagonal preconditioning		Current preconditioning	
	RHS norm	Krylov iteration	RHS norm	Krylov iteration	RHS norm	Krylov iteration
Trial step	5.9E-03	7839	5.9E-03	4	5.9E-03	4
Iteration 1	1.9E-01	2575	1.9E-01	4	1.9E-01	4
Iteration 5	1.1E-03	7335	1.1E-03	4	1.1E-03	4
Iteration 10	7.5E-10	6951	7.5E-10	4	7.5E-10	4
Solve time (s)	3.10	0.16		0.16		

hydro-mechanical systems [85] as,

$$\mathbf{S}_{\mathrm{M}} = \mathbf{K}_{D} - \alpha \mathbf{M}, \text{ where } \mathbf{M} = \begin{bmatrix} \mathbf{M}_{p_{\mathrm{L}}} & \mathbf{0} \\ \mathbf{0} & \mathbf{M}_{T} \end{bmatrix} \text{ with } [\mathbf{M}_{\pi}]_{e}^{a,b} = \int_{\mathcal{B}} N_{a} N_{b} dV, \quad (\pi = p_{\mathrm{L}}, T).$$
 (80)

Here, we choose  $\mathbf{K}_D$  with matrices at diagonal positions ( $\mathbf{C}$  and  $\mathbf{F}$ ) to simplify and improve the calculations based on physics point of view (assuming weak coupling between pressure and temperature) [85,87,88]. In addition, M is the extended mass matrix including liquid water pressure and temperature fields. The methods to estimate the optimal coefficient  $\alpha$  and the approximation of  $A^{-1}$  and  $S^{-1}$  for the block Krylov solver in isothermal poromechanics problem can be found in [85,93]. Note that it is also possible to estimate an optimal choice of  $\alpha$  for thermo-hydro-mechanical problems. In such a case, the parameter  $\alpha$  should be different for each block to deliver the optimal performance. One feasible strategy can be found in the interesting works done by White et al. [93] and Kim [94], where the relationship of the operator-split solvers (fixed stress split (e.g., [95]); adiabatic split (e.g., [96])) can be exploited for the pre-conditioners. The improvement of preconditioning strategy for thermo-hydro-mechanical formulation will be considered in the future. Nevertheless, based on the evidences collected from the numerical experiments, even the simple preconditioning strategy in (Eq. (79)) has already provided significant improvement in efficiency for THM solvers. In these numerical tests, we adopt the thawing consolidation problem as a benchmark to evaluate the efficiency of the preconditioning strategy within the infinitesimal deformation range. The detailed problem descriptions are provided in Section 6.1. Due to the difference in scales of the tangential term with respect to the displacement (e.g., tangential stiffness), pore pressure (e.g., hydraulic conductivity) and temperature (e.g., thermal conductivity), the thawing consolidation may lead to a highly nonlinear problem whose consistent tangents can be very ill-conditioned (i.e., with a very high condition number).

To evaluate the efficiency of different preconditioning strategies, we first introduce a coarse mesh (the total number of unknowns is 120 with 72 degrees of freedoms for displacement, 24 for liquid water pressure and another 24 for the temperature fields) and solve the corresponding system of equations with and without applying the pre-conditioners. The number of iterations required to obtain the converged solution from the solver without any no-preconditioning strategy is compared against the counterparts in which two different preconditioning strategies are used (Table 1). For comparison purposes, in addition to the pre-conditioner introduced in Eq. (80), we implement a simpler block-diagonal pre-conditioner where each diagonal block is separately inverted and no Schur-complement approximation is introduced, which is one of the simplest approaches one might use in practice. The preconditioning strategy for the current study saves the calculation time by reducing the Krylov iterations. Regardless of whether a preconditioner is used, the norm of the residual obtained after each Newton iteration step is identical as expected. Although there is no significant difference between the diagonal and current preconditioning strategies, the number of Krylov iterations is significantly reduced in both cases — an indication that both pre-conditioners are effective for this simple problem.

To analyze how mesh refinement affects the performance of the pre-conditioners, we re-run the numerical experiments with a finer mesh (the total number of unknowns is 420 with 252 degrees of freedoms for displacement, 84 for liquid water pressure and another 84 for the temperature fields). In this case, the solver without any pre-conditioner does not yield converged solution within 50,000 iterations with the same tolerance  $(10^{-9})$ . However, the solvers equipped with either pre-conditioner is still able to deliver converged solution, as shown in Table 2. This result also indicates that the pre-conditioner in Eq. (80) outperforms the simpler diagonal pre-conditioner. It requires less Krylov iterations in each Newton–Raphson step and is approximately 48% faster. Both numerical experiments indicate the importance of pre-conditioners on the solver performance.

Table 2 Residence norm (square root of the inner product of residual column vector) and the number of Krylov iterations at the selected Newton steps for comparison of preconditioning strategy (refined mesh condition with the total degrees of freedom 420) – No preconditioning case does not yield converged solution within 50,000 iterations with the same tolerance ( $10^{-9}$ ).

Newton steps	Diagonal precondition	oning	Current preconditio	ning
	RHS norm	Krylov iteration	RHS norm	Krylov iteration
Trial step	1.6E-02	38	1.6E-02	13
Iteration 1	1.6E-01	19	1.6E-01	15
Iteration 5	1.9E-03	16	1.9E-03	13
Iteration 10	7.4E-10	17	7.4E - 10	13
Solve time (s)	10.2		5.28	

#### 6. Numerical simulations

We conducted four numerical examples to test the applicability and robustness of the proposed thermo-hydromechanical model for frozen soil. Through these models, we analyze the geometrical effect during thawing by comparing results from infinitesimal and finite strain simulations. We demonstrate how the plastic dissipation influences the three-phase frozen porous medium at finite deformation range, and validate our predictions with experimental results. The first two examples are selected to analyze and validate the simulated phase-transition effect during the freezing and thawing processes. In the first example, we idealize the frozen soil deposit as a one dimensional domain subjected to an increased temperature at the top of the surface with drained boundary condition. Due to the temperature difference, heat flux developing on the top of the deposit leads to the thawing and therefore the ground consolidates until the steady state is reached. In another related example, we decrease the temperature at the top surface of an unfrozen soil deposit so that the outflow heat flux may instead lead to the freezing process starting at the top and developing through depth of the domain. The third example is adopted a well injection problem. We formulate the frozen ground with a well at the center and apply both pore flux and temperature gradient to mimic the injection of hot water. In the last example, we examine the formation of shear band and the influence of plastic dissipation in a biaxial compression test. We vary the Taylor-Quinney coefficient and re-run the simulations to obtain the axial stressdisplacement curve of the sample and analyze the effect of plastic dissipation. In addition, we obtain the shear band under different combinations of thermal conductivity and permeability to see how thermal and hydraulic couplings influence the regularization of THM formulation for frozen porous media.

## 6.1. Thawing consolidation of frozen ground

In this numerical example, we simulate a thawing consolidation process of frozen ground by a raised temperature prescribed at the top surface. The purpose of this example is to validate the numerical model and demonstrate the performance of numerical formulation when phase transition from crystal ice to liquid water occurs. It should be noted that other experimental data such as those reported in [97] can also be used for validation purpose. We discretize the three-dimensional domain and fix the displacement at the bottom and radial surfaces to simulate a 1-D consolidation induced by thawing. The domain of frozen soil sample has a height of 10 cm and a cross-section of  $0.3 \times 0.3$  cm<sup>2</sup> following the previous experimental set up by Yao et al. [98].

Fig. 4(a) shows the schematic diagram and test conditions. The initial temperature of the domain except the top surface is -1 °C and the surcharge load of 50 kPa is applied. Meanwhile, the temperature at the top surface is prescribed to be 20 °C with a drained condition by imposing zero pore pressure. The bottom end is kept at -1 °C and the radial surfaces are insulated and assumed to be undrained to consolidate only through the top surface. As a result of this setup, thawing consolidation progresses in time until a new isothermal status is reached. The material properties of solid, liquid water and crystal ice used in the simulations including the hydraulic conductivity of  $7.0 \times 10^{-9}$  m/s can be found in detail from [98].

Fig. 4(b) shows the thawing settlement results obtained from both infinitesimal and finite strain simulations. In addition, the experimental results along with the previous numerical analyses performed by Yao et al. [98] are also presented in the same figure. This simulation is performed under the elastic range and we obtained the settlement at the top surface along with time. Both current infinitesimal and finite strain model show good agreement with the previous experiment data. Furthermore, the infinitesimal strain model predicts larger vertical settlement compared to the corresponding finite strain model due to the geometrical non-linearity effect (e.g., [99]).

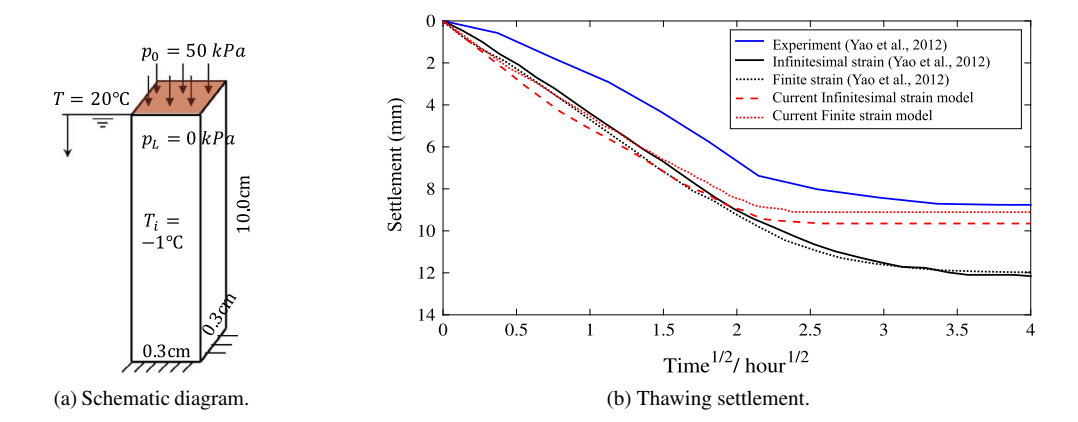


Fig. 4. Schematic diagram of thawing simulation with boundary conditions (a) and the comparison of thawing settlement results (b) with the previous research [98].

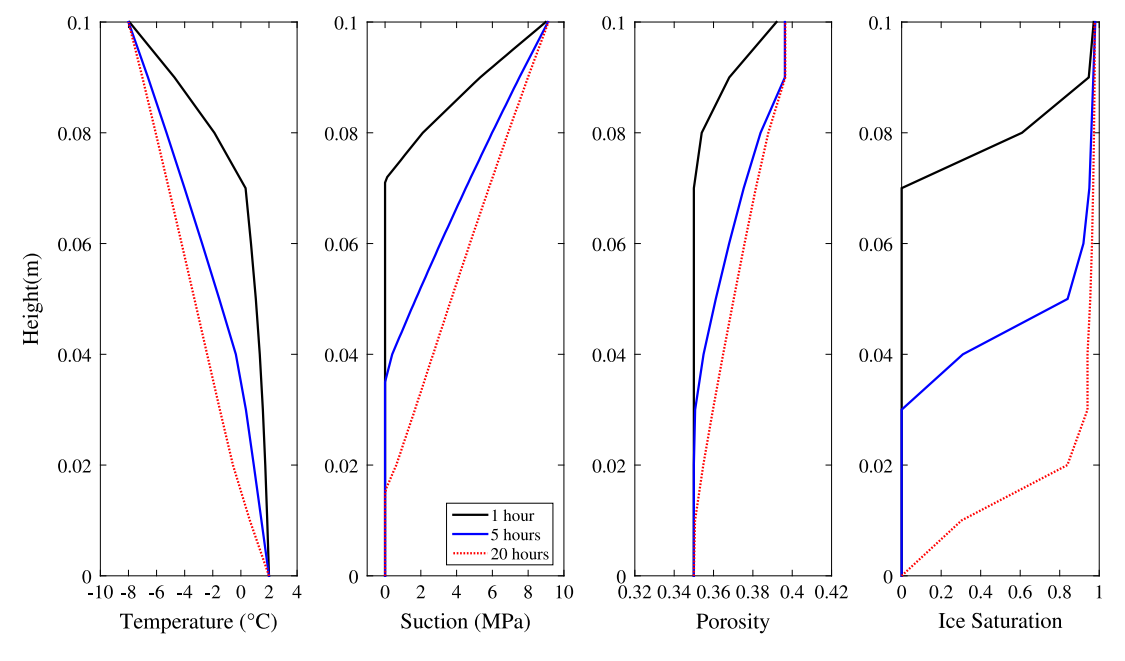


Fig. 5. Transient responses of the freezing soil — changes of temperature, cryo-suction, porosity and ice saturation.

#### 6.2. Soil freezing from unfrozen state

In addition to the thawing simulation, the soil freezing test under 1-D heat flux condition is also conducted to check the numerical implementation regarding phase transition from unfrozen to frozen states. This example can be considered as an opposite situation of the previous numerical experiment of which the concept is adopted from the previous study by Zhou [32]. Likewise in the schematic in Fig. 4, we formulated three dimensional domain and fixed the bottom and radial surface displacement. With the initially unfrozen condition with temperature of 2 °C, we lower the temperature at the top to -2 °C so that the freezing process mobilizes to downward. The temperature at the bottom surface is fixed with 2 °C and the radial surfaces are insulated. Table 3 describes the input parameters used in this numerical simulation. We prescribed the impermeable boundary conditions except the bottom surface with drained condition ( $p_L = 0$ ) to allow water supply.

The first column in Fig. 5 shows the temperature profile along the depth in different times. We can see that the temperature reaches the steady state after 20 h. The second column shows the suction pressure profile with different

**Table 3**Reference input parameters of homogeneous numerical model for material sensitivity test.

Parameter	Description	Value	Unit
$\rho_{\mathrm{S}}$	Mass density of solid	2.7	Mg/m <sup>3</sup>
$ ho_{ m L}$	Mass density of liquid water	1.0	$Mg/m^3$
$ ho_{ m C}$	Mass density of crystal ice	0.9	$Mg/m^3$
$c_{\mathrm{S}}$	Specific heat of solid	900	kJ/Mg/K
$c_{ m L}$	Specific heat of liquid water	4180	kJ/Mg/K
$c_{\mathrm{C}}$	Specific heat of crystal ice	2100	kJ/Mg/K
$\kappa_{\mathrm{S}}$	Thermal conductivity of solid	$3.0 \times 10^{-3}$	kW/m/K
$\kappa_{ m L}$	Thermal conductivity of water	$0.6 \times 10^{-3}$	kW/m/K
$\kappa_{\mathrm{C}}$	Thermal conductivity of crystal ice	$2.2 \times 10^{-3}$	kW/m/K
$\phi$	Initial porosity	0.3	_
k	Intrinsic permeability	$1.0 \times 10^{-12}$	$m^2$
$\mu_0$	Viscosity (at 0 °C)	$1.8 \times 10^{-6}$	kPa s
$c_r$	Recompression index	0.035	_
$c_c$	Compression index	0.30	_

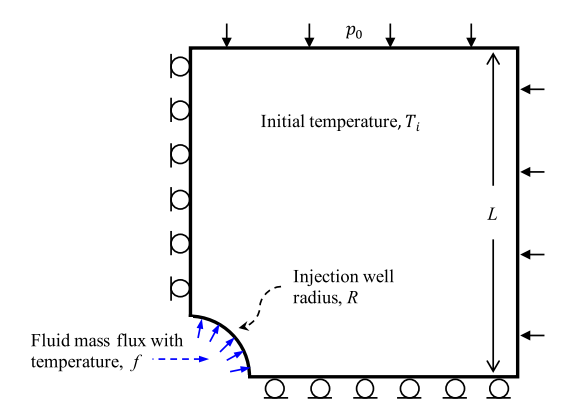


Fig. 6. Schematics of injection well simulation: a quarter of the domain (the domain length, L=0.38 m; the radius of injection well, R=0.03 m; the confining pressure,  $p_0=100$  kPa) was simulated from the initial temperature ( $T_i$ ) of -2 °C. The temperature of the fluid mass flux (f=0.001 cm<sup>2</sup>/s) was increased to 1 °C.

times in depth. It is observed that cryo-suction due to freezing is developed and progressed downward along the time. In addition, frost heaving or volume expansion due to freezing in frozen porous medium is captured through the change of porosity in the third column. The last column shows how the freezing fringe changes along with time through the ice saturation profile.

#### 6.3. Injecting unfrozen fluid in frozen ground

To demonstrate the forward-prediction capacity of the proposed model, an injection well problem is replicated numerically. Fig. 6 shows the schematics of the current problem. Due to rotational symmetry, only a quarter of the domain is considered. The domain is defined by the length (L) of 0.38 m and the injection well radius (R) of 0.03 m. The initial temperature condition was set to -2 °C. The outer boundaries are assumed to be impermeable and insulated and mechanically confined with the pressure  $(p_0)$  of 100 kPa. We assumed the type of frozen soil as a lightly overconsolidated clay (OCR = 1.5), and the mechanical, hydraulic and thermal properties are described in Table 4.

We conducted the preliminary test prescribing the fluid flux without temperature change, and the constant mass flux of 0.001 cm<sup>2</sup>/s. was selected which had little influence (no equivalent plastic strain) on the domain during the given time (up to 10 h from the initial state). Then we prescribed the fluid mass flux with temperature increase around the well surface to induce the inelastic behavior vicinity of the well causing the plastic deformation. First of all, we compare the numerical results from infinitesimal and finite strain models. Fig. 7 presents the thermo-hydromechanical behavior of injection well at different time for each model. As expected, phase transition zones expand

Table 4

Mechanical, hydraulic and thermal input parameters for injection well problem.

Parameter	Description	Value	Unit
$\rho_{\mathrm{S}}$	Mass density of solid	2.7	Mg/m <sup>3</sup>
$ ho_{ m L}$	Mass density of liquid water	1.0	$Mg/m^3$
$ ho_{ m C}$	Mass density of crystal ice	0.9	$Mg/m^3$
$c_{\mathrm{S}}$	Specific heat of solid	900	kJ/Mg/K
$c_{ m L}$	Specific heat of liquid water	4190	kJ/Mg/K
$c_{\mathrm{C}}$	Specific heat of crystal ice	2095	kJ/Mg/K
$\kappa_{ m S}$	Thermal conductivity of solid	$1.27 \times 10^{-3}$	kW/m/K
$\kappa_{ m L}$	Thermal conductivity of water	$5.80 \times 10^{-3}$	kW/m/K
κc	Thermal conductivity of crystal ice	$2.20 \times 10^{-3}$	kW/m/K
$\phi$	Initial porosity	0.3	_
k	Intrinsic permeability	$1.0 \times 10^{-15}$	$m^2$
$\mu_0$	Viscosity (at 0 °C)	$1.8 \times 10^{-6}$	kPa s
$c_r$	Recompression index	0.03	_
$c_c$	Compression index	0.13	_
$p_c$	Preconsolidation stress	150	kPa

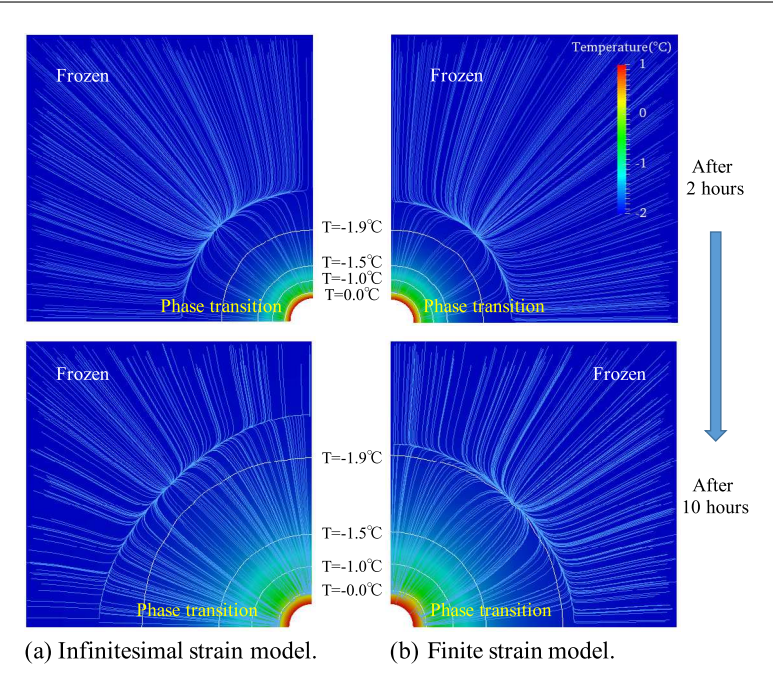


Fig. 7. Thermo-hydro-mechanical behavior of frozen soil in the injection well problem — different phase zones indicated by the temperature contour and liquid water stream line under (a) infinitesimal and (b) finite strain models.

after 10 h from the initial state due to heat transfer. The increase of temperature makes the crystal ice thawing into liquid water as predicted by the freezing characteristic function (in Eq. (37)), which leads to the change of liquid water pressure reflected on stream line configuration. Therefore, we can see the different phases from both the temperature contour and the hydraulic stream line induced by injecting unfrozen water around the well surface. With respect to the comparison of infinitesimal and finite strain model, we can see the little difference in heat transfer from temperature contours. However, the expansion of liquid water stream line is delayed in finite strain model compared to that from the infinitesimal model. This can be explained by the effect of geometrical nonlinearity, as we observed in Section 6.1 that the finite strain model estimates less settlement due to geometrical nonlinear effect (e.g., [98,99]). The more distinct difference between the infinitesimal and finite strain models is observed as the time progresses (Fig. 7).

Next we analyze the effect of latent heat reflected on apparent heat capacity. In the concept of apparent heat capacity, the freezing characteristic function is introduced into heat capacity to incorporate the phase transition effect

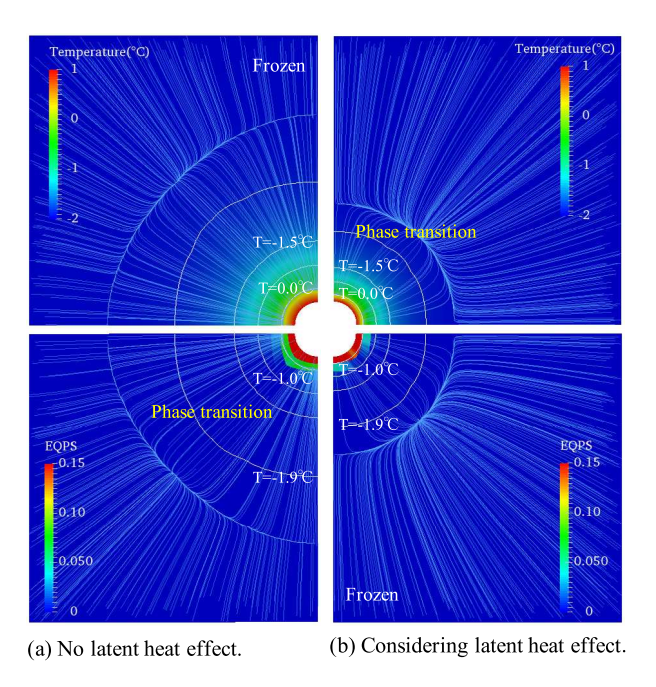


Fig. 8. The effect of considering latent heat in apparent specific heat on thermo-hydro-mechanical behavior of frozen soil. Temperature and equivalent plastic strain distribution with fluid flow stream line is compared at the same time (after 2 h from the initial state).

in the energy balance equation (Eq. (23)). Therefore, the effective specific heat of the frozen soil system changes along the temperature change. When the temperature ranges around 0.0 to -2.0 where the freezing characteristic function shows significant changes, the increase of effective specific heat of the system delays the heat transfer to account for the latent heat effect in phase transition. We note that the effect of latent heat due to phase transition is evaluated qualitatively. This consideration may play an important role in changes of temperature profile with time diffuse and related pore pressure distributions, elastic and inelastic behaviors for the frozen soil (e.g., [100,101]). Fig. 8 shows how the apparent heat capacity influences the heat transfer and the frozen soil system. At the same time step, the heat transfer develops much faster when the latent heat effect is not considered. These are depicted both on temperature contour line and liquid water stream line. Moreover, as the phase transition zone further expands under the no latent heat effect model, the higher equivalent plastic strain is concentrated around the well surface. This can be further explained from the constitutive model (Eq. (31)), which includes the temperature change upon the yield surface size due to the cryo-suction. In other words, the increase of temperature accelerates the plastic behavior by shrinking the yield surface as a recursive process. We further present the influence of latent heat effect on the mechanical behavior along the time in Fig. 9. Along with the prescribed temperature boundary condition, the changes of temperature around 0.03 m away from the well surface with time are described in Fig. 9(a) to evaluate the consideration of latent heat. While the region around the well surface becomes unfrozen state in 1 h when the latent heat is ignored, the heat transfer is delayed and the well surface region stays below 0 °C until around 5 h after the initial state when the latent heat is considered. This is also reflected on cryo-suction pressure changes in Fig. 9(b). The displacement and equivalent plastic strain results in Fig. 9(c) and (d) further identify the recursive process between the temperature increase and yield surface change. In other words, the more inelastic behavior around the well surface is observed in a shorter time when latent heat effect is not considered. However, the heat transfer delay due to latent heat effect causes less concentration of equivalent plastic strain by procrastinating the change of yield surface against temperature change.

## 6.4. Thermal softening by plastic dissipation in 2D biaxial test

In this section, we analyze how the plastic dissipation in frozen soil influences the mechanical behavior using numerical experiments. The plastic dissipation may generate heat due to frictional movement of soils in the shear

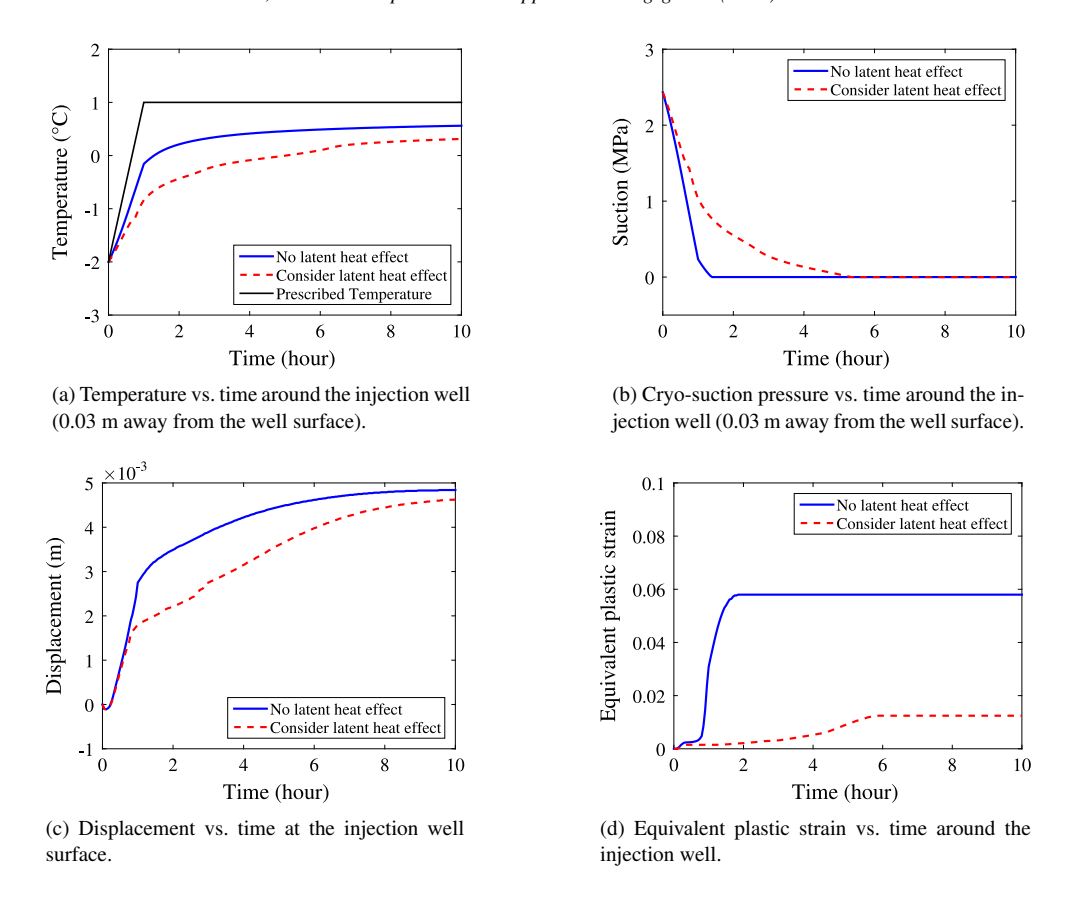


Fig. 9. The effect of considering latent heat in apparent specific heat on thermo-hydro-mechanical behavior of frozen soil: displacement vs. time at the well surface, cryo-suction, temperature and equivalent plastic strain vs. time around the injection well (0.03 m away from the well surface).

band. We set up the numerical simulation for 2D biaxial test (Fig. 10). The top boundary moves downwards uniformly with the rate of 0.0002 m/s, while a constant confining pressure of  $\sigma_c = 1000$  kPa is applied on the right side of the specimen. The bottom of the specimen is fixed, and the left side is fixed along the lateral direction for shear band initiation. The gravity is neglected for this small specimen to simplify the problem. The specimen is globally undrained and thus no-fluid-flux boundary conditions are prescribed. All four surfaces are thermally insulated with no-thermal-flux condition. In other words, no Dirichlet boundary condition is adopted for both liquid water pressure and temperature fields. The mechanical, hydraulic and thermal properties of frozen soil were used based on the injection well problem (Table 4), but the preconsolidation stress ( $p_c$ ) of 3000 kPa was adopted.

In general, the loading rate needs to be fast enough so that we can see the effect of heat generation due to mechanical dissipation. Otherwise, the heat generated would reach the steady state condition before it acts. Fig. 11 indicates how the shear band is formed using the equivalent plastic strain (at 80 s) and related temperature distributions to identify the effect of plastic dissipation, which leads to heat generation. We use the Taylor–Quinney coefficient  $\beta$  to control the plastic dissipation in the energy balance equation (28). When the plastic dissipation is considered ( $\beta = 1.0$ , Fig. 11(b)), the increase of temperature and heat transfer are observed around the shear band, while no heat generation occurs when the plastic dissipation is totally ignored ( $\beta = 0.0$ , Fig. 11(c)). Considering the freezing characteristic function and mechanical constitutive model we used in this study, it can be expected that the increase of temperature leads to shrinking of the size of the yield surface. Fig. 12(a) shows how the local yield surface changes due to heat generation including the local stress path at two indicated points. Initially at Point 1, the stress path moves upward vertically (Path 1) due to the location of element and globally undrained boundary conditions with low permeability of the specimen. When the stress path reaches the yield surface, the shrinking of yield surface because of heat generation enforces the stress path to follow the trajectory described in Path 1 of Fig. 12(a). At Point 2, the similar behavior is

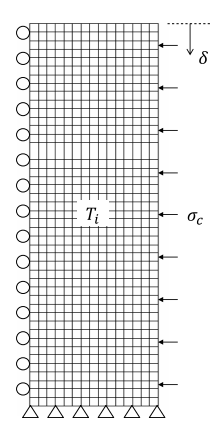


Fig. 10. The schematic of the 2D biaxial test with the dimensions of 0.1 m  $\times$  0.3 m deforming in plane strain: the vertical displacement ( $\delta$ ) is applied on the top surface of the specimen, while the bottom of the specimen is fixed; the left side is fixed in the lateral direction; the confining pressure ( $\sigma_c$ ) of 1000 kPa is applied on the right side of the specimen. The initial temperature ( $T_i$ ) was set to -1 °C.

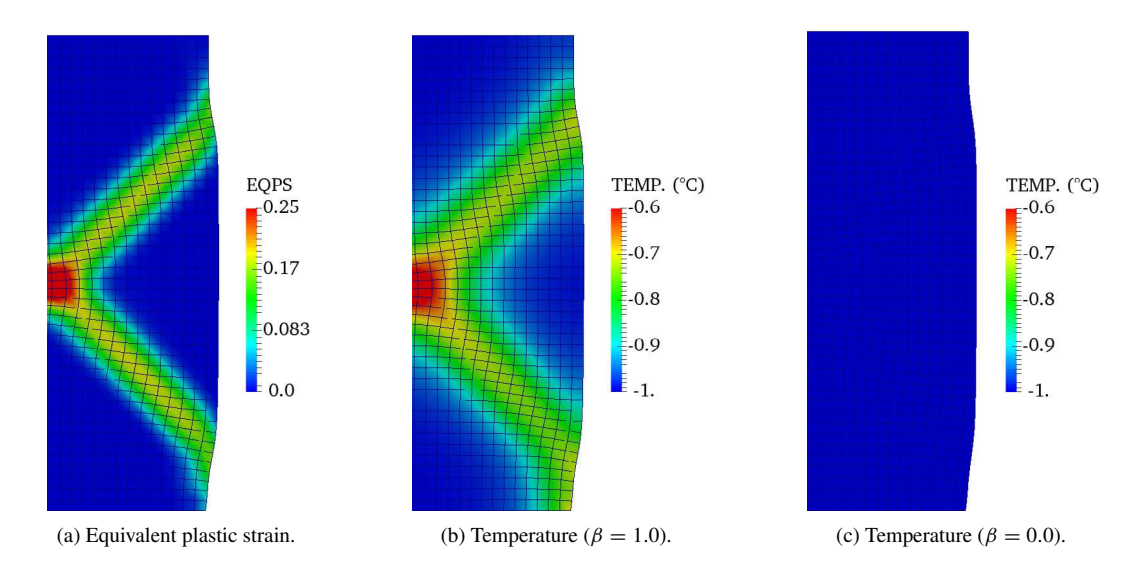


Fig. 11. The effect of plastic dissipation in 2D biaxial test: Equivalent plastic strain forming shear band (a) at 80 s and the temperature distribution with different Taylor–Quinney coefficients ((b)  $\beta = 1.0$ , (c)  $\beta = 0.0$  – no dissipation) in a deformed shape (scale = 1.0).

observed but its stress path changes before hitting the yield surface (Path 2). Due to the location of the element, the local liquid water pressure changes in the elastic regime even though the boundary conditions are globally undrained. We can further analyze the local behavior in Fig. 12(b). In the selected elements, the local deviatoric stress—strain behaviors are observed along with the volume changes. The thermal softening comes from the change of yield surface due to temperature increase along the shear band. The deviatoric stress—strain curves on Point 1 and 2 give the similar behavior. However, due to the mean effective stress changes in Point 2 with Path 2, the volume expansion shows different in Point 2 compared to Point 1. The specific volume changes including temperature changes are depicted in Fig. 12(c). Both curves of the specific volume-logarithm of -p' do not encounter the critical state line of -1.0 °C which changes with the temperature. The higher increase of temperature at Point 1 compared to Point 2 is also identified.

We can further evaluate the effect of plastic dissipation in terms of the stress-strain behavior of frozen soil specimen. The vertical stress and axial strain obtained at the top of the specimen are presented in Fig. 13(a). Here we include additional test results with slow loading rate of  $2.0 \times 10^{-7}$  m/s. When the dissipation effect is ignored

Table 5

Mechanical, hydraulic and thermal input parameters for injection well problem.

Parameter	Low	Reference	High
Thermal conductivity (kW/m/K) Intrinsic permeability (m <sup>2</sup> )	$3.0 \times 10^{-6} \\ 1.0 \times 10^{-20}$	$3.0 \times 10^{-3} \\ 1.0 \times 10^{-15}$	$3.0 \times 10^{0}$ $1.0 \times 10^{-10}$

 $(\beta = 0)$ , the hardening behavior is captured in the given range of axial strain (<5%). However, the fast loading case  $(2.0 \times 10^{-4} \text{ m/s})$  with plastic dissipation effects leads to the strain softening behavior after the axial strain increases more than 3%. Considering the local element behavior (in Fig. 13), the thermal softening due to shrinking of yield surfaces with temperature increase is reflected on the specimen behavior. When the slow loading rate is adopted  $(2.0 \times 10^{-7} \text{ m/s})$ , however, the vertical stress of the specimen follows the no dissipation case ( $\beta = 0$ ) with slight decrease of stress values. In other words, the decrease of loading rate allows the heat to transfer fast enough which leads to the minor increase of temperature around the shear band. The increase of temperature with the slow loading rate was less than 0.05 °C. Note that the mechanical constitutive model is rate independent. However, the proposed framework captures the effect of loading rate by including the mechanical dissipation as well as coupled governing equations for thermo-hydro-mechanical interactions. In addition, we present the volume change in the specimen using the porosity distribution (Fig. 13(b)). Note that the porosity distribution of slow loading rate shows little difference compared to the no dissipation case. As can be seen, the strain localization and increase of porosity are concentrated around the shear band when the loading rate is slow (or when thermal dissipation is ignored). However, the increase of porosity from other parts as well as shear band in the specimen are observed when the plastic dissipation is considered. This indicates that the contribution of heat transfer from the temperature increase along the shear band leads to thermal softening by affecting the yield surface change.

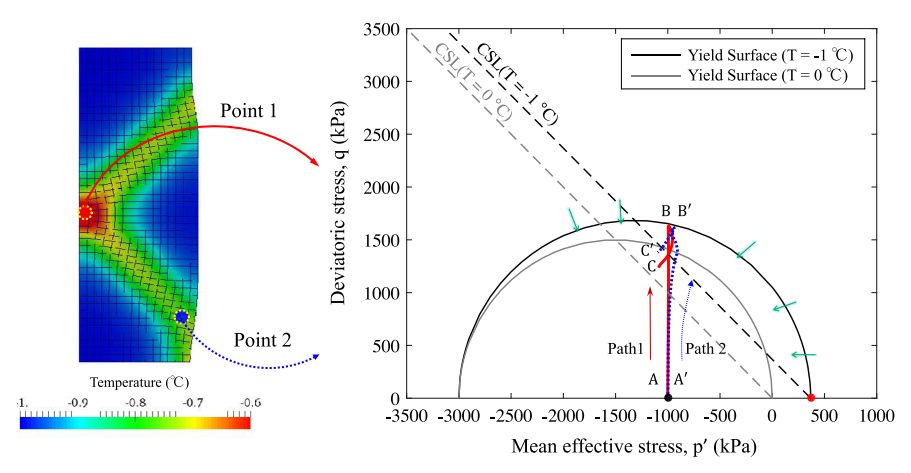
#### 6.5. Thermo-hydro-mechanical coupling effects of frozen soil system on shear band

The frozen soil system formulated in this study is not in an isothermal condition and the phase transition between the liquid water and crystal ice is considered. Thus, solid response is affected by both thermal and hydraulic couplings. As studied in the previous researches (e.g., [14,15,102]), shear band width is influenced by the thermal diffusivity as well as diffusivity of the pore fluid. To identify how thermal and hydraulic diffusivities influence the thermo-hydromechanical responses of frozen soil which include phase transition, we conducted a parametric study by changing the permeability and thermal conductivity.

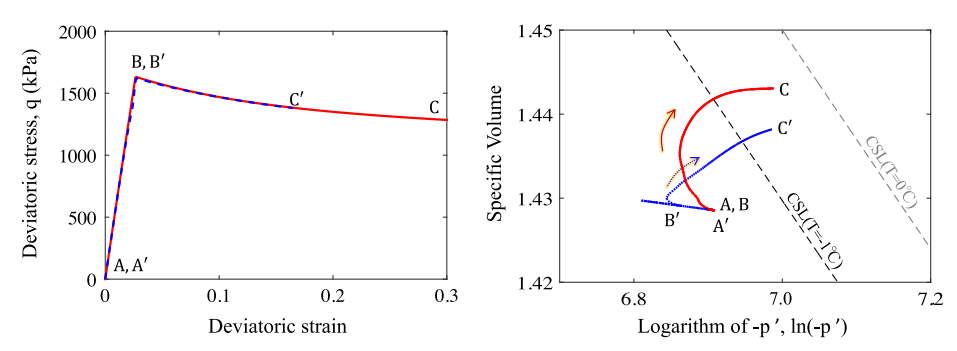
The numerical experiment is set up based on the 2D biaxial test conducted in the previous section (Section 6.4). Likewise, Fig. 10 shows the schematics of the test while the confining stress ( $\sigma_c$ ) of 500 kPa was used. The same rate of moving boundary condition (0.0002 m/s) was used on the top of the specimen. Note that the drained condition was applied on the top and bottom surfaces of the specimen to allow liquid water flow. Table 5 presents a set of intrinsic permeability and thermal conductivity of frozen soil. First we hold the permeability as the reference value and evaluate the effect of thermal conductivity by comparing the low and high values. Next we fix the thermal conductivity with the reference value and analyze shear band with low and high permeability.

Fig. 14 demonstrates equivalent plastic strain, temperature distribution and the pore pressure at 150 s after the loading. The equivalent plastic strain results in the formation of shear band under the high (left) and low (high) thermal conductivities. The onset of shear bands locates slightly different in both cases, but the concentration of equivalent plastic strain and shape of shear bands show little difference. The temperature distribution due to generation of heat by the local plastic dissipation on shear bands differs, however, because of thermal conductivity difference. As expected, the high thermal conductivity leads heat transfer much faster as in Fig. 14(b). The pore pressure increase shows little difference while the stream line of liquid fluid follows the onset of shear band (Fig. 14(c)). In this numerical experiment, the change of thermal diffusivity may affect the location and thickness of shear band due to heat transfer.

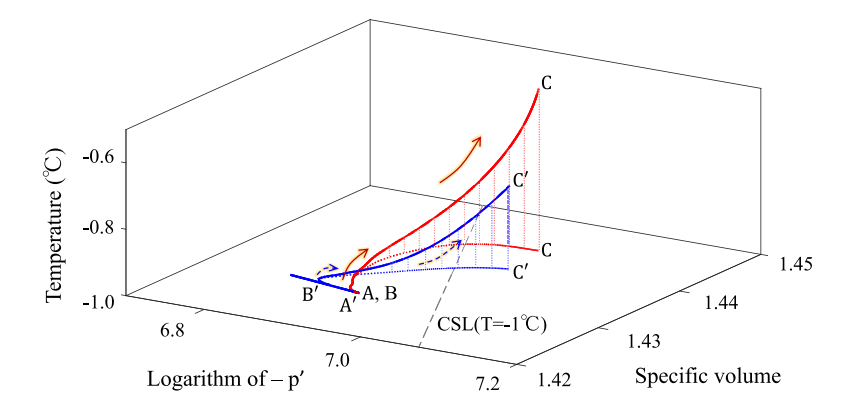
Next we fix the thermal conductivity and change the permeability. Fig. 15 demonstrates equivalent plastic strain, temperature distribution and the liquid water pressure at 150 s after the loading with different permeability conditions. The little difference in initiation and formation of the shear band is observed. However, a marginally thicker shear banding and lower concentration of equivalent plastic strain is identified under the high permeability condition (Fig. 15(a)). In addition, slightly faster heat transfer is captured, which can be considered as convection effect in



(a) The change of yield surface and stress paths at two different local elements due to increase of temperature by plastic dissipation (Point 1 with Path 1: A–B–C, and Point 2 with Path 2: A′–B′–C′).



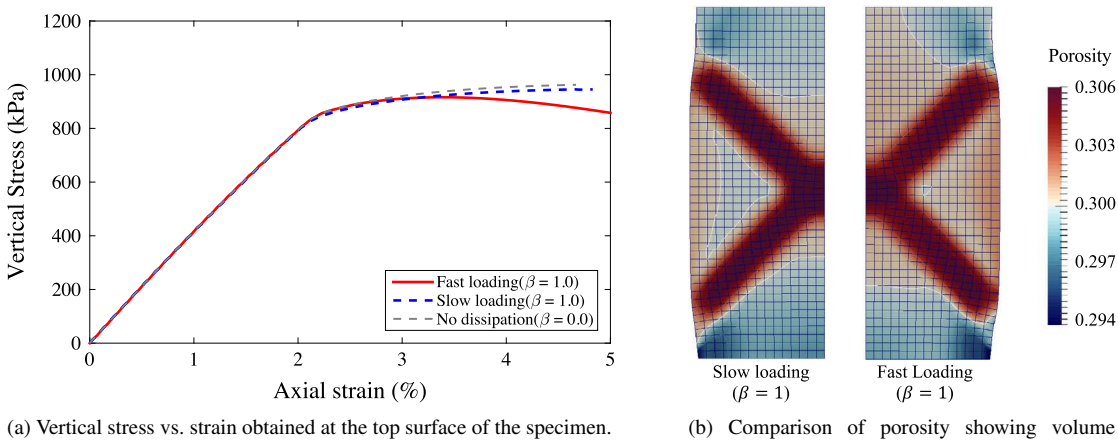
(b) The deviatoric stress vs. deviatoric strain curve and specific volume vs. logarithm of means effective stress  $(\ln(-p'))$  curves at the two local elements (Path 1: A–B–C and Path 2: A'–B'–C').



(c) The behavior of specific volumes with respect to logarithm of means effective stress  $(\ln(-p'))$  including temperature change (following the trajectory of A–B–C and A'–B'–C').

Fig. 12. The effect of plastic dissipation in 2D biaxial test: the change of yield surface, stress path, deviatoric stress vs. strain and specific volume vs. logarithm of mean effective stress at two different local elements.

energy balance equation (Fig. 15(b)). By considering the temperature increase and yield surface change reflected on the solid constitutive model of this framework, the heat transfer accelerated by convection effects may contribute the size of shear band. The difference in permeability is identified from the results of pore pressure in Fig. 15(c), where the most excess pore pressure generated by loading is dissipated.



change in the specimen.

Fig. 13. The effect of plastic dissipation reflected on the specimen. Fast and slow loading indicates  $2.0 \times 10^{-4}$  m/s and  $2.0 \times 10^{-7}$  m/s, respectively.

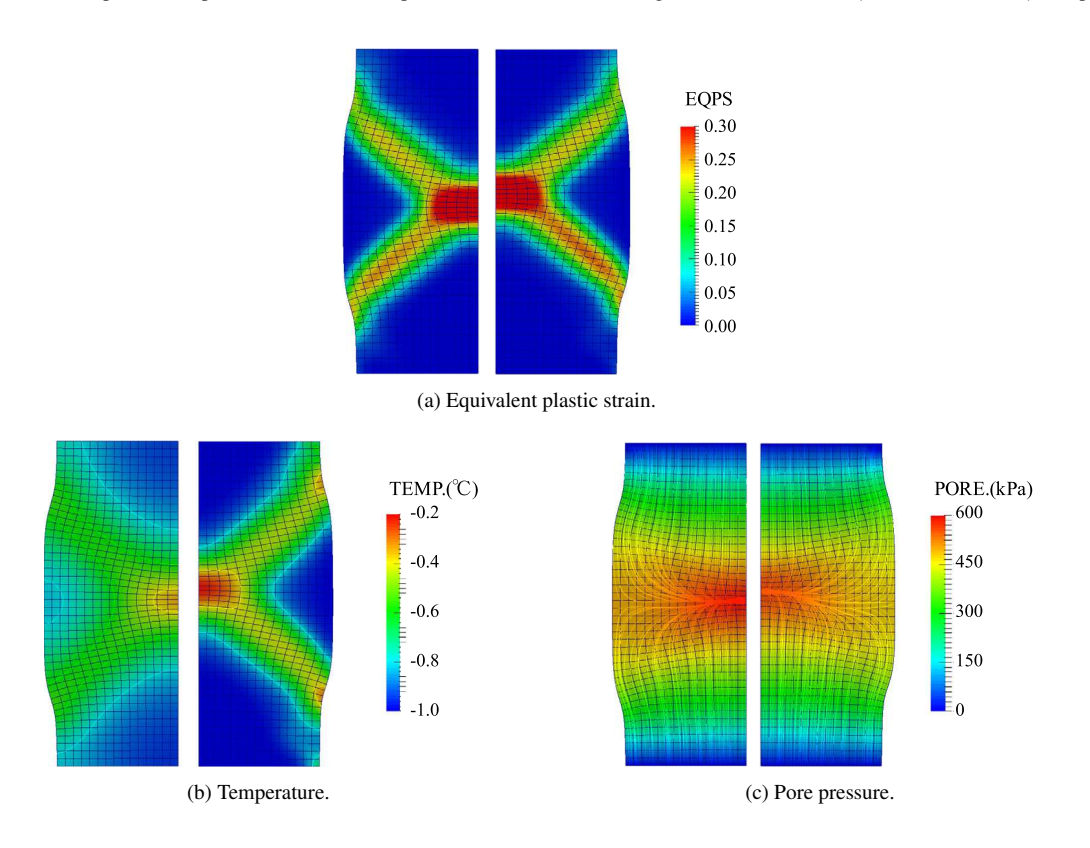


Fig. 14. The effect of different thermal conductivities on shear band (equivalent plastic strain, temperature and pore pressure distributions): the left and right figures in (a), (b) and (c) present the results under high and low thermal conductivities, respectively.

#### 7. Conclusions

In this study, we present, for the first time, a computational framework that simulates the thermo-hydro-mechanical responses of freezing and thawing porous media in the finite deformation range. Our starting point is the mixture and pre-melting theory, which enables one to derive finite strain constitutive laws for both the path-dependent solid, hydraulic and thermal constitutive responses. On the theoretical side, we analyze how the degree of saturation of

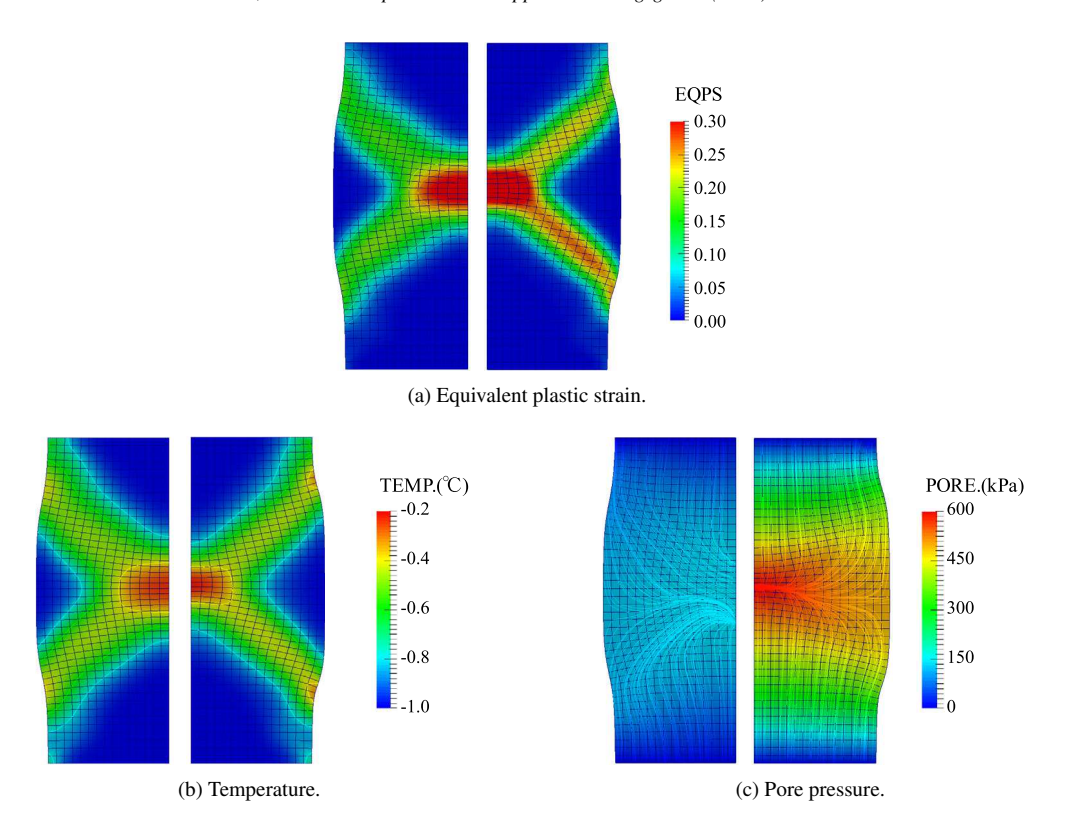


Fig. 15. The effect of different permeability on the development shear band (equivalent plastic strain, temperature and pore pressure distributions): the left and right figures in (a), (b) and (c) present the results under high and low effective permeabilities, respectively.

ice, determined from the unfrozen pore water pressure and temperature, introduces nonlocality and rate dependence to the non-mechanical hardening/softening mechanism. Unlike the single-physics solid mechanics problem in which strain and strain history alone are sufficient to predict stress, the incorporation of non-mechanical hardening makes the solid skeleton constitutive responses to be highly sensitive to the evolution of the pore water pressure, temperature and the corresponding gradients. As a result, any simplification made on the balance principles, such as eliminating the heat generated by the plastic dissipation in the balance of energy and neglecting the heat convection terms, may have profound impacts on the quality of predictions on the solid mechanical behavior. On the computational side, we address the major difficulties encountered in modeling the frozen porous media. In particular, the lack of the two-fold inf–sup condition, usage of preconditioner, and the logarithmic and exponential mapping techniques used for implementing the finite-strain constitutive law are explicated. In summary, this work provides a feasible approach to model frozen porous media with unfrozen water constituents and addresses some key theoretical and computational issues for capturing the essence of the path-dependent thermo-hydro-mechanical responses of porous media.

## Acknowledgments

This research is supported by the Earth Materials and Processes program at the US Army Research Office under grant contract W911NF-14-1-0658, W911NF-15-1-0442 and W911NF-15-1-0581, Sandia National Laboratories under grant contract 1557089 as well as the Mechanics of Material program at National Science Foundation under grant contract CMMI-1462760. These supports are gratefully acknowledged. The authors thank Drs. Jinhyun Choo and Joshua A. White for making their finite element code base Geocentric available to the authors and for fruitful discussions, and the three anonymous reviewers for their helpful suggestions and comments.

## **Appendix**

In this section, we present the expressions of  $3 \times 3$  Jacobian in Eq. (73). Note that the displacement, liquid water pressure and temperature fields are approximated as,

$$\boldsymbol{u}^h = \boldsymbol{N}^u \boldsymbol{d}, \quad \boldsymbol{p}_1^h = \boldsymbol{N}^p \boldsymbol{p}_1, \quad \boldsymbol{T}^h = \boldsymbol{N}^T \boldsymbol{T}. \tag{A.81}$$

where a superscript h is used to indicate spatially discretized values;  $N^u$ ,  $N^p$  and  $N^T$  are shape function matrices for displacement, liquid water pressure and temperature, respectively; d,  $p_L$  and T are corresponding nodal vectors. Following the standard Galerkin approximations, the weighting functions are represented as,

$$\eta^h = N^u c, \quad \varphi^h = N^p \bar{c}, \quad \theta^h = N^T \tilde{c}.$$
(A.82)

Recall the Jacobian in Eq. (73),

$$\begin{bmatrix} \mathbf{A} & \mathbf{B}_1 & \mathbf{D}_1 \\ \mathbf{B}_2 & \mathbf{C} & \mathbf{E}_1 \\ \mathbf{D}_2 & \mathbf{E}_2 & \mathbf{F} \end{bmatrix}, \tag{A.83}$$

where each block matrix consists of the linearization (Section 4.2) can be expressed as follows.

$$\mathbf{A} = -\int_{\mathcal{B}} (\nabla^{X} N^{u})^{\mathrm{T}} : \mathbf{A} : (\nabla^{X} N^{u}) dV + \int_{\mathcal{B}} (\nabla^{X} N^{u})^{\mathrm{T}} : (\bar{p} \mathbf{F}^{-\mathrm{T}}) (J \nabla^{X} N^{u} : \mathbf{F}^{-\mathrm{T}}) dV - \int_{\mathcal{B}} (\nabla^{X} N^{u})^{\mathrm{T}} : \left[ \bar{p} J (\mathbf{F}^{-\mathrm{T}} \cdot (\nabla^{X} N^{u})^{\mathrm{T}} \cdot \mathbf{F}^{-\mathrm{T}}) \right] dV,$$
(A.84)

$$\mathbf{B}_{1} = \int_{\mathcal{B}} (\nabla^{X} N^{u})^{\mathrm{T}} : \left( J \frac{\partial \bar{p}}{\partial p_{\mathrm{L}}} \mathbf{F}^{-\mathrm{T}} \right) N^{p} dV, \tag{A.85}$$

$$\mathbf{D}_{1} = \int_{\mathcal{B}} (\nabla^{X} N^{u})^{\mathrm{T}} : \left( J \frac{\partial \bar{p}}{\partial T} \mathbf{F}^{-\mathrm{T}} \right) N^{T} dV, \tag{A.86}$$

$$\mathbf{B}_{2} = \int_{\mathcal{B}} (N^{p})^{\mathrm{T}} \left[ (1 - \phi^{\mathrm{S}})(\rho_{\mathrm{L}} - \rho_{\mathrm{C}}) \dot{S}_{\mathrm{L}} \right] (J \nabla^{X} N^{u} : \mathbf{F}^{-\mathrm{T}}) dV 
+ \int_{\mathcal{B}} (N^{p})^{\mathrm{T}} \left[ \rho_{\mathrm{L}} S_{\mathrm{L}} + \rho_{\mathrm{C}} (1 - S_{\mathrm{L}}) \right] (\nabla^{X} \dot{\mathbf{u}} : \mathbf{F}^{-\mathrm{T}}) (J \nabla^{X} N^{u} : \mathbf{F}^{-\mathrm{T}}) dV 
+ \int_{\mathcal{B}} (N^{p})^{\mathrm{T}} \left[ \rho_{\mathrm{L}} S_{\mathrm{L}} + \rho_{\mathrm{C}} (1 - S_{\mathrm{L}}) \right] (J \nabla^{X} N^{u} : \mathbf{F}^{-\mathrm{T}}) dV 
- \int_{\mathcal{B}} (N^{p})^{\mathrm{T}} \left[ \rho_{\mathrm{L}} S_{\mathrm{L}} + \rho_{\mathrm{C}} (1 - S_{\mathrm{L}}) \right] \left[ J \nabla^{X} \dot{\mathbf{u}} : (\mathbf{F}^{-\mathrm{T}} \cdot (\nabla^{X} N^{u})^{\mathrm{T}} \cdot \mathbf{F}^{-\mathrm{T}}) \right] dV 
+ \int_{\mathcal{B}} (\nabla^{X} N^{p})^{\mathrm{T}} \cdot \left[ (\rho_{\mathrm{L}} \mathbf{F}^{-1} \cdot \mathbf{k} \cdot \mathbf{F}^{-\mathrm{T}}) \cdot (\nabla^{X} p_{\mathrm{L}}) \right] (J \nabla^{X} N^{u} : \mathbf{F}^{-\mathrm{T}}) dV 
- \int_{\mathcal{B}} (\nabla^{X} N^{p})^{\mathrm{T}} \cdot \left[ \rho_{\mathrm{L}} J \mathbf{F}^{-1} \cdot (\nabla^{X} N^{u}) \cdot \mathbf{F}^{-1} \right] \cdot (\mathbf{k} \cdot \mathbf{F}^{-\mathrm{T}}) \cdot (\nabla^{X} p_{\mathrm{L}}) dV 
\int_{\mathcal{B}} (\nabla^{X} N^{p})^{\mathrm{T}} \cdot (\rho_{\mathrm{L}} J \mathbf{F}^{-1} \cdot \mathbf{k}) \cdot \left[ \mathbf{F}^{-\mathrm{T}} \cdot (\nabla^{X} N^{u})^{\mathrm{T}} \cdot \mathbf{F}^{-\mathrm{T}} \right] \cdot (\nabla^{X} p_{\mathrm{L}}) dV \tag{A.87}$$

$$\mathbf{C} = \int_{\mathcal{B}} (N^{p})^{\mathrm{T}} \left[ J(1 - \phi^{\mathrm{S}})(\rho_{\mathrm{L}} - \rho_{\mathrm{C}}) \left( \frac{\partial \dot{S}_{\mathrm{L}}}{\partial p_{\mathrm{L}}} \right) \right] N^{p} dV$$

$$+ \int_{\mathcal{B}} (N^{p})^{\mathrm{T}} \left[ (\rho_{\mathrm{L}} - \rho_{\mathrm{C}}) \left( \frac{\partial \dot{S}_{\mathrm{L}}}{\partial p_{\mathrm{L}}} \right) (J \nabla^{X} \dot{\boldsymbol{u}} : \boldsymbol{F}^{-\mathrm{T}}) \right] N^{p} dV ,$$

$$+ \int_{\mathcal{B}} (\nabla^{X} N^{p})^{\mathrm{T}} \cdot \left[ \rho_{\mathrm{L}} J \boldsymbol{F}^{-1} \cdot \left( \frac{\partial \boldsymbol{k}}{\partial p_{\mathrm{L}}} \right) \cdot \boldsymbol{F}^{-\mathrm{T}} \right] \cdot (\nabla^{X} p_{\mathrm{L}}) N^{p} dV$$

$$+ \int_{\mathcal{B}} (\nabla^{X} N^{p})^{\mathrm{T}} \cdot \left( \rho_{\mathrm{L}} J \boldsymbol{F}^{-1} \cdot \boldsymbol{k} \cdot \boldsymbol{F}^{-\mathrm{T}} \right) \cdot (\nabla^{X} N^{p}) dV , \tag{A.88}$$

$$\begin{split} \mathbf{E}_{1} &= \int_{\mathcal{B}} (N^{p})^{\mathrm{T}} \left[ J(1 - \phi^{S})(\rho_{L} - \rho_{C}) \left( \frac{\partial S_{L}}{\partial T} \right) \right] N^{T} dV \\ &+ \int_{\mathcal{B}} (N^{p})^{\mathrm{T}} \left[ (\rho_{L} - \rho_{C}) \left( \frac{\partial S_{L}}{\partial T} \right) (J \nabla^{X} \dot{u} : F^{-\mathrm{T}}) \right] N^{T} dV, \\ &+ \int_{\mathcal{B}} (\nabla^{X} N^{p})^{\mathrm{T}} \cdot \left[ \rho_{L} J F^{-1} \cdot \left( \frac{\partial k}{\partial T} \right) \cdot F^{-\mathrm{T}} \right] \cdot (\nabla^{X} p_{L}) N^{T} dV, \\ &+ \int_{\mathcal{B}} (\nabla^{X} N^{T})^{\mathrm{T}} \cdot \left[ \rho_{L} J F^{-1} \cdot \left( \frac{\partial k}{\partial T} \right) \cdot F^{-\mathrm{T}} \right] \cdot (\nabla^{X} p_{L}) N^{T} dV, \\ &+ \int_{\mathcal{B}} (\nabla^{X} N^{T})^{\mathrm{T}} \cdot \left[ J F^{-1} \cdot \kappa \cdot F^{-\mathrm{T}} \right) \cdot (\nabla^{X} T) \right] (J \nabla^{X} N^{u} : F^{-\mathrm{T}}) dV \\ &- \int_{\mathcal{B}} (\nabla^{X} N^{T})^{\mathrm{T}} \cdot \left[ J F^{-1} \cdot \kappa \cdot (F^{-\mathrm{T}} \cdot (\nabla^{X} N^{u}) \cdot F^{-\mathrm{T}}) \cdot (\nabla^{X} T) dV \\ &- \int_{\mathcal{B}} (\nabla^{X} N^{T})^{\mathrm{T}} \cdot \left[ J F^{-1} \cdot \kappa \cdot (F^{-\mathrm{T}} \cdot (\nabla^{X} N^{u}) \cdot F^{-\mathrm{T}}) \right] \cdot (\nabla^{X} T) dV \\ &- \int_{\mathcal{B}} (\nabla^{X} N^{T})^{\mathrm{T}} \cdot \left[ J F^{-1} \cdot \kappa \cdot (F^{-\mathrm{T}} \cdot (\nabla^{X} N^{u}) \cdot F^{-\mathrm{T}}) \right] \cdot (\nabla^{X} T) dV \\ &+ \int_{\mathcal{B}} (N^{T})^{\mathrm{T}} \left( \frac{\phi^{L} S_{L} c p_{L}}{\rho_{L}} \right) \rho_{L} \left[ (F^{-1} \cdot k \cdot F^{-\mathrm{T}}) (J \nabla^{X} N^{u} : F^{-\mathrm{T}}) \right] \\ &- J (F^{-1} \cdot (\nabla^{X} N^{u}) \cdot F^{-\mathrm{T}}) \cdot (\kappa \cdot F^{-\mathrm{T}}) \cdot (\nabla^{X} T) dV \\ &- \int_{\mathcal{B}} (N^{T})^{\mathrm{T}} \left( \frac{\phi^{L} S_{L} c p_{L}}{\rho_{L}} \right) \left[ W \cdot (F^{-\mathrm{T}} \cdot (\nabla^{X} N^{u}) \cdot F^{-\mathrm{T}}) \cdot (\nabla^{X} T) \right] dV, \end{aligned}$$

$$\mathbf{E}_{2} = \int_{\mathcal{B}} (N^{T})^{\mathrm{T}} \left( J \dot{T} \frac{\partial c p}{\partial p_{L}} \right) N^{p} dV + \int_{\mathcal{B}} (\nabla^{X} N^{T})^{\mathrm{T}} \cdot \left[ \frac{\partial K T (\kappa)}{\partial p_{L}} \cdot (\nabla^{X} T) \right] N^{p} dV \\ &+ \int_{\mathcal{B}} (\nabla^{X} N^{T})^{\mathrm{T}} \cdot \left[ \left( \frac{\phi^{L} S_{L} c p_{L}}{\rho_{L}} \right) \left( \frac{\partial W (k_{T})}{\partial p_{L}} \right) \cdot F^{-\mathrm{T}} \cdot (\nabla^{X} T) \right] N^{p} dV \\ &+ \int_{\mathcal{B}} (\nabla^{X} N^{T})^{\mathrm{T}} \cdot \left[ \left( \frac{\phi^{L} S_{L} c p_{L}}{\rho_{L}} \right) \left( \frac{\partial W (k_{T})}{\partial p_{L}} \right) \cdot F^{-\mathrm{T}} \cdot (\nabla^{X} T) \right] N^{T} dV \\ &+ \int_{\mathcal{B}} (N^{T})^{\mathrm{T}} \left[ \left( \frac{\phi^{L} S_{L} c p_{L}}{\rho_{L}} \right) \left( \frac{\partial W (k_{T})}{\partial T} \right) \cdot F^{-\mathrm{T}} \cdot (\nabla^{X} T) \right] N^{T} dV \\ &+ \int_{\mathcal{B}} (N^{T})^{\mathrm{T}} \left[ \left( \frac{\phi^{L} S_{L} c p_{L}}{\rho_{L}} \right) \left( \frac{\partial W (k_{T})}{\partial T} \right) \cdot F^{-\mathrm{T}} \cdot (\nabla^{X} T) \right] N^{T} dV \\ &+ \int_{\mathcal{B}} (N^{T})^{\mathrm{T}} \left[ \left( \frac{\phi^{L} S_{L} c p_{L}}{\rho_{L}} \right) \left( \frac{\partial W (k_{T})}{\partial T} \right) \cdot F^{-\mathrm{T}}$$

#### References

- [1] S.A. Shoop, S.R. Bigl, Moisture migration during freeze and thaw of unsaturated soils: modeling and large scale experiments, Cold Reg. Sci. Technol. 25 (1) (1997) 33–45.
- [2] O. Coussy, Poromechanics of freezing materials, J. Mech. Phys. Solids 53 (8) (2005) 1689–1718.

- [3] A.W. Rempel, J.S. Wettlaufer, M.G. Worster, Premelting dynamics in a continuum model of frost heave, J. Fluid Mech. 498 (2004) 227–244
- [4] S.A. Shoop, R. Affleck, R. Haehnel, V. Janoo, Mechanical behavior modeling of thaw-weakened soil, Cold Reg. Sci. Technol. 52 (2) (2008) 191–206.
- [5] D. Wisser, S. Marchenko, J. Talbot, C. Treat, S. Frolking, Soil temperature response to 21st century global warming: the role of and some implications for peat carbon in thawing permafrost soils in North America, Earth Syst. Dyn. 2 (1) (2011) 121–138.
- [6] R.L. Michalowski, M. Zhu, Frost heave modeling using porosity rate function, Int. J. Numer. Anal. Methods Geomech. 30 (8) (2006) 703–722.
- [7] S. Nishimura, A. Gens, S. Olivella, R.J. Jardine, THM-coupled finite element analysis of frozen soil: formulation and application, Géotechnique 59 (3) (2009) 159–171.
- [8] H.L. Jessberger, Theory and application of ground freezing in civil engineering, Cold Reg. Sci. Technol. 3 (1) (1980) 3–27.
- [9] J.M. McKenzie, C.I. Voss, D.I. Siegel, Groundwater flow with energy transport and water–ice phase change: numerical simulations, benchmarks, and application to freezing in peat bogs, Adv. Water Resour. 30 (4) (2007) 966–983.
- [10] O. Coussy, P. Monteiro, Unsaturated poroelasticity for crystallization in pores, Comput. Geotech. 34 (4) (2007) 279–290.
- [11] A. Belotserkovets, J.H. Prévost, Thermoporoelastic response of a fluid-saturated porous sphere: An analytical solution, Internat. J. Engrg. Sci. 49 (12) (2011) 1415–1423.
- [12] M.M. Zhou, G. Meschke, A three-phase thermo-hydro-mechanical finite element model for freezing soils, Int. J. Numer. Anal. Methods Geomech. 37 (18) (2013) 3173–3193.
- [13] M. Mikkola, J. Hartikainen, Mathematical model of soil freezing and its numerical implementation, Internat. J. Numer. Methods Engrg. 52 (5–6) (2001) 543–557.
- [14] W. Sun, A stabilized finite element formulation for monolithic thermo-hydro-mechanical simulations at finite strain, Internat. J. Numer. Methods Engrg. 103 (11) (2015) 798–839.
- [15] S. Na, W. Sun, Wave propagation and strain localization in a fully saturated softening porous medium under the non-isothermal conditions, Int. J. Numer. Anal. Methods Geomech. 40 (10) (2016) 1485–1510. http://dx.doi.org/10.1002/nag.2505.
- [16] A. Gens, Soil-environment interactions in geotechnical engineering, Géotechnique 60 (1) (2010) 3-74.
- [17] J.S. Wettlaufer, M.G. Worster, Premelting dynamics, Annu. Rev. Fluid Mech. 38 (2006) 427–452.
- [18] K.S. Henry, A Review of the Thermodynamics of Frost Heave, Technical Report, DTIC Document, 2000.
- [19] O.C. Zienkiewicz, A.H.C. Chan, M. Pastor, B.A. Schrefler, T. Shiomi, Computational Geomechanics, Wiley Chichester, 1999.
- [20] W. Ehlers, J. Bluhm, Porous Media: Theory, Experiments and Numerical Applications, Springer Science & Business Media, 2013.
- [21] H. Wang, Theory of Linear Poroelasticity with Applications to Geomechanics and Hydrogeology, Princeton University Press, 2000.
- [22] L. Dormieux, D. Kondo, F.J. Ulm, Microporomechanics, John Wiley & Sons, 2006.
- [23] K. Wang, W. Sun, Anisotropy of a Tensorial Bishop's coefficient for wetted granular materials, J. Eng. Mech. (2015) B4015004.
- [24] K. Wang, W. Sun, A semi-implicit discrete-continuum coupling method for porous media based on the effective stress principle at finite strain, Comput. Methods Appl. Mech. Eng. 304 (2016) 546–583.
- [25] K. Wang, W. Sun, A semi-implicit micropolar discrete-to-continuum method for granular materials, in: M. Papadrakakis, V. Papadopoulos, G. Stefanou, V. Plevris (Eds.), Proceedings of European Congress on Computational Methods in Applied Science and Engineering, June, Crete Island, 2016, pp. 5–10.
- [26] A.W. Bishop, G.E. Blight, Some aspects of effective stress in saturated and partly saturated soils, Géotechnique 13 (3) (1963) 177–197.
- [27] D.G. Fredlund, H. Rahardjo, Soil Mechanics for Unsaturated Soils, John Wiley & Sons, 1993.
- [28] M. Frémond, F. Maceri, Mechanics, Models and Methods in Civil Engineering, vol. 61, Springer Science & Business Media, 2011.
- [29] B.A. Schrefler, The Finite Element Method in Soil Consolidation (Ph.D. thesis), University College of Swansea, 1984.
- [30] K. O'Neill, The physics of mathematical frost heave models: A review, Cold Reg. Sci. Technol. 6 (3) (1983) 275–291.
- [31] K. O'Neill, R.D. Miller, Exploration of a rigid ice model of frost heave, Water Resour. Res. 21 (3) (1985) 281–296.
- [32] M.M. Zhou, Computational Simulation of Soil Freezing: Multiphase Modeling and Strength Upscaling (Ph.D. thesis), Ruhr University Bochum, 2013.
- [33] L. Sanavia, B.A. Schrefler, P. Steinmann, A formulation for an unsaturated porous medium undergoing large inelastic strains, Comput. Mech. 28 (2) (2002) 137–151.
- [34] S. Diebels, W. Ehlers, Dynamic analysis of a fully saturated porous medium accounting for geometrical and material nonlinearities, Internat. J. Numer. Methods Engrg. 39 (1) (1996) 81–97.
- [35] J.C. Simo, Numerical analysis and simulation of plasticity, in: Handbook of Numerical Analysis, 1998, pp. 183-499.
- [36] W. Ehlers, Foundations of multiphasic and porous materials, in: Porous Media, Springer, 2002, pp. 3–86.
- [37] W. Sun, J.T. Ostien, A.G. Salinger, A stabilized assumed deformation gradient finite element formulation for strongly coupled poromechanical simulations at finite strain, Int. J. Numer. Anal. Methods Geomech. 37 (16) (2013) 2755–2788.
- [38] X. Song, R.I. Borja, Mathematical framework for unsaturated flow in the finite deformation range, Internat. J. Numer. Methods Engrg. 97 (9) (2014) 658–682.
- [39] J.E. Andrade, R.I. Borja, Modeling deformation banding in dense and loose fluid-saturated sands, Finite Elem. Anal. Des. 43 (5) (2007)
- [40] R.L. Michalowski, A constitutive model of saturated soils for frost heave simulations, Cold Reg. Sci. Technol. 22 (1) (1993) 47–63.
- [41] J.C. Simo, C. Miehe, Associative coupled thermoplasticity at finite strains: formulation, numerical analysis and implementation, Comput. Methods Appl. Mech. Eng. 98 (1) (1992) 41–104.
- [42] L.E. Goodrich, An introductory review of numerical methods for ground thermal regime calculations, in: Paper, Division of Building Research, National Research Council Canada (1061), 1982, p. 32.

- [43] K. Hansson, J. Šimŭnek, M. Mizoguchi, L.C. Lundin, M.T. van Genuchten, Water flow and heat transport in frozen soil, Vadose Zone J. 3 (2) (2004) 693–704.
- [44] J. Côté, J.M. Konrad, A generalized thermal conductivity model for soils and construction materials, Can. Geotech. J. 42 (2) (2005) 443–458.
- [45] G.I. Taylor, H. Quinney, The latent energy remaining in a metal after cold working, Proc. R. Soc. A 143 (849) (1934) 307–326.
- [46] L. Stainier, M. Ortiz, Study and validation of a variational theory of thermo-mechanical coupling in finite visco-plasticity, Int. J. Solids Struct. 47 (5) (2010) 705–715.
- [47] M. Arriaga, C. McAuliffe, H. Waisman, Instability analysis of shear bands using the instantaneous growth-rate method, Int. J. Impact Eng. 87 (2016) 156–168.
- [48] R.I. Borja, C. Tamagnini, Cam-clay plasticity part III: Extension of the infinitesimal model to include finite strains, Comput. Methods Appl. Mech. Eng. 155 (1) (1998) 73–95.
- [49] C. Callari, F. Auricchio, E. Sacco, A finite-strain cam-clay model in the framework of multiplicative elasto-plasticity, Int. J. Plast. 14 (12) (1998) 1155–1187.
- [50] D. Gallipoli, A. Gens, R. Sharma, J. Vaunat, An elasto-plastic model for unsaturated soil incorporating the effects of suction and degree of saturation on mechanical behavior, Géotechnique 53 (1) (2003) 123–136.
- [51] R. Nova, R. Castellanza, C. Tamagnini, A constitutive model for bonded geomaterials subject to mechanical and/or chemical degradation, Int. J. Numer. Anal. Methods Geomech. 27 (9) (2003) 705–732.
- [52] C. Tamagnini, R. Castellanza, R. Nova, A generalized backward Euler algorithm for the numerical integration of an isotropic hardening elastoplastic model for mechanical and chemical degradation of bonded geomaterials, Int. J. Numer. Anal. Methods Geomech. 26 (10) (2002) 963–1004.
- [53] A. Cuitino, M. Ortiz, A material-independent method for extending stress update algorithms from small-strain plasticity to finite plasticity with multiplicative kinematics, Eng. Comput. 9 (4) (1992) 437–451.
- [54] E.A. de Souza Neto, D. Peric, D.R.J. Owen, Computational Methods for Plasticity: Theory and Applications, John Wiley & Sons, 2011.
- [55] R.I. Borja, Plasticity: Modeling & Computation, Springer Science & Business Media, 2013.
- [56] R.I. Borja, On the mechanical energy and effective stress in saturated and unsaturated porous continua, Int. J. Solids Struct. 43 (6) (2006) 1764–1786
- [57] R.I. Borja, C. Tamagnini, A. Amorosi, Coupling plasticity and energy-conserving elasticity models for clays, Journal of Geotechnical and Geoenvironmental Engineering 123 (10) (1997) 948–957.
- [58] E.E. Alonso, A. Gens, A. Josa, et al., Constitutive model for partially saturated soils, Géotechnique 40 (3) (1990) 405–430.
- [59] R. Butterfield, A natural compression law for soils (an advance on  $e \log p'$ ), Géotechnique 29 (4) (1979).
- [60] K. Hashiguchi, Elasto-plastic constitutive laws of granular materials, constitutive equations of soils, in: Proc. Spec. Session 9 of 9th Int. ICSMFE, 1977, pp. 73–82.
- [61] K. Hashiguchi, On the linear relations of  $v \ln p$  and  $\ln v \ln p$  for isotropic consolidation of soils, Int. J. Numer. Anal. Methods Geomech. 19 (5) (1995) 367–376.
- [62] R.W.R. Koopmans, R.D. Miller, Soil freezing and soil water characteristic curves, Soil Sci. Am. J. 30 (6) (1966) 680-685.
- [63] Ebert J.A. Spaans, John M. Baker, The soil freezing characteristic: Its measurement and similarity to the soil moisture characteristic, Soil Science Society of America Journal 60 (1) (1996) 13–19.
- [64] M.T. van Genuchten, A closed-form equation for predicting the hydraulic conductivity of unsaturated soils, Soil Sci. Am. J. 44 (5) (1980) 892–898.
- [65] L. Luckner, M.T. van Genuchten, D.R. Nielsen, A consistent set of parametric models for the two-phase flow of immiscible fluids in the subsurface, Water Resour. Res. 25 (10) (1989) 2187–2193.
- [66] S.A. Grant, Physical and Chemical Factors Affecting Contaminant Hydrology in Cold Environments, Technical Report, DTIC Document, 2000.
- [67] G.A. Holzapfel, Nonlinear Solid Mechanics. A Continuum Approach for Engineering, West Sussex, England: John Wiley & Sons, Ltd, 2000.
- [68] R.I. Borja, E. Alarcón, A mathematical framework for finite strain elastoplastic consolidation Part 1: Balance laws, variational formulation, and linearization, Comput. Methods Appl. Mech. Engrg. 122 (1) (1995) 145–171.
- [69] W. Sun, Q. Chen, J.T. Ostien, Modeling the hydro-mechanical responses of strip and circular punch loadings on water-saturated collapsible geomaterials, Acta Geotech. (2013).
- [70] P. Mira, M. Pastor, T. Li, X. Liu, A new stabilized enhanced strain element with equal order of interpolation for soil consolidation problems, Comput. Methods Appl. Mech. Eng. 192 (37) (2003) 4257–4277.
- [71] J. Choo, R.I. Borja, Stabilized mixed finite elements for deformable porous media with double porosity, Comput. Methods Appl. Mech. Eng. 293 (2015) 131–154.
- [72] R.W. Lewis, B.A. Schrefler, The Finite Element Method in the Static and Dynamic Deformation and Consolidation of Porous Media, John Wiley, 1998.
- [73] J.A. White, R.I. Borja, Stabilized low-order finite elements for coupled solid-deformation/fluid-diffusion and their application to fault zone transients, Comput. Methods Appl. Mech. Engrg. 197 (49) (2008) 4353–4366.
- [74] R. Liu, M.F. Wheeler, C.N. Dawson, R. Dean, Modeling of convection-dominated thermoporomechanics problems using incomplete interior penalty Galerkin method, Comput. Methods Appl. Mech. Eng. 198 (9) (2009) 912–919.
- [75] P.B. Bochev, C.R. Dohrmann, M.D. Gunzburger, Stabilization of low-order mixed finite elements for the Stokes equations, SIAM J. Numer. Anal. 44 (1) (2006) 82–101.
- [76] J.S. Howell, N.J. Walkington, Inf-sup conditions for twofold saddle point problems, Numer. Math. 118 (4) (2011) 663-693.
- [77] K. Bathe, Finite Element Procedures, Klaus-Jurgen Bathe, 2006.
- [78] D. Chapelle, K. Bathe, The inf-sup test, Comput. Struct. 47 (4) (1993) 537–545.

- [79] K. Bathe, A. Iosilevich, D. Chapelle, An inf-sup test for shell finite elements, Comput. Struct. 75 (5) (2000) 439-456.
- [80] K. Bathe, The inf-sup condition and its evaluation for mixed finite element methods, Comput. Struct. 79 (2) (2001) 243-252.
- [81] W. Sun, A. Mota, A multiscale overlapped coupling formulation for large-deformation strain localization, Comput. Mech. (2014) 1–18.
- [82] K. Bathe, D. Hendriana, F. Brezzi, G. Sangalli, Inf-sup testing of upwind methods, Internat. J. Numer. Methods Engrg. 48 (2000) 745-760.
- [83] W. Sun, Z. Cai, J. Choo, Mixed Arlequin method for multiscale poromechanics problems, Internat. J. Numer. Methods Engrg. (2016).
- [84] D. Pantuso, K. Bathe, A four-node quadrilateral mixed-interpolated element for solids and fluids, Math. Models Methods Appl. Sci. 5 (8) (1995) 1113–1128.
- [85] J.A. White, R.I. Borja, Block-preconditioned Newton-Krylov solvers for fully coupled flow and geomechanics, Comput. Geosci. 15 (4) (2011) 647-659.
- [86] M. Ferronato, G. Gambolati, P. Teatini, Ill-conditioning of finite element poroelasticity equations, Int. J. Solids Struct. 38 (34) (2001) 5995–6014.
- [87] W. Bangerth, R. Hartmann, G. Kanschat, Deal. II—a general-purpose object-oriented finite element library, ACM Trans. Math. Softw. 33 (4) (2007) 24.
- [88] W. Bangerth, T. Heister, L. Heltai, G. Kanschat, M. Kronbichler, M. Maier, B. Turcksin, T.D. Young, The deal. II library, Version 8 (2013) 1–5.
- [89] C. Burstedde, L.C. Wilcox, O. Ghattas, p4est: Scalable algorithms for parallel adaptive mesh refinement on forests of octrees, SIAM J. Sci. Comput. 33 (3) (2011) 1103–1133.
- [90] M.A. Heroux, J.M. Willenbring, A new overview of the Trilinos project, Sci. Program. 20 (2) (2012) 83–88.
- [91] C.N. Dawson, H. Klíe, M.F. Wheeler, C.S. Woodward, A parallel, implicit, cell-centered method for two-phase flow with a preconditioned Newton–Krylov solver, Comput. Geosci. 1 (3–4) (1997) 215–249.
- [92] J.W. Demmel, N.J. Higham, R.S. Schreiber, Stability of block LU factorization, Numer. Linear Algebra Appl. 2 (2) (1995) 173–190.
- [93] J.A. White, N. Castelletto, H.A. Tchelepi, Block-partitioned solvers for coupled poromechanics: A unified framework, Comput. Methods Appl. Mech. Engrg. 303 (2016) 55–74.
- [94] J. Kim, Unconditionally stable sequential schemes for thermoporomechanics: Undrained-adiabatic and extended fixed-stress splits, in: SPE Reservoir Simulation Symposium, Society of Petroleum Engineers, 2015.
- [95] J. Kim, H.A. Tchelepi, R. Juanes, Stability, accuracy, and efficiency of sequential methods for coupled flow and geomechanics, SPE J. 16 (2) (2011) 249–262.
- [96] F. Armero, J.C. Simo, A new unconditionally stable fractional step method for non-linear coupled thermomechanical problems, Int. J. Numer. Methods Eng. 35 (4) (1992) 737–766.
- [97] S. Zhang, D. Sheng, G. Zhao, F. Niu, Z. He, Analysis of frost heave mechanisms in a high-speed railway embankment, Can. Geotech. J. 53 (3) (2015) 520–529.
- [98] X. Yao, J. Qi, W. Wu, Three dimensional analysis of large strain thaw consolidation in permafrost, Acta Geotech. 7 (3) (2012) 193–202.
- [99] C. Li, R.I. Borja, R.A. Regueiro, Dynamics of porous media at finite strain, Comput. Methods Appl. Mech. Eng. 193 (36) (2004) 3837–3870.
- [100] D. Mottaghy, V. Rath, Latent heat effects in subsurface heat transport modeling and their impact on palaeotemperature reconstructions, Geophys. J. Int. 164 (1) (2006) 236–245.
- [101] D.M. Anderson, A.R. Tice, H.L. McKim, The unfrozen water and the apparent specific heat capacity of frozen soils, in: North American Contribution, Second International Conference on Permafrost, National Academy of Science, Yakutsk, USSR, Washington, DC, 1973, pp. 289–295.
- [102] H.W. Zhang, L. Sanavia, B.A. Schrefler, An internal length scale in dynamic strain localization of multiphase porous media, Mech. Cohesive Fract. Mater. 4 (5) (1999) 443–460.